



Supermassive Black Holes with High Accretion Rates in Active Galactic Nuclei. XIII. Ultraviolet Time Lag of H β Emission in Mrk 142

Viraja C. Khatu¹, Sarah C. Gallagher¹, Keith Horne², Edward M. Cackett³, Chen Hu⁴, Sofia Pasquini⁵, Patrick Hall⁶,
Jian-Min Wang⁴, Wei-Hao Bian⁷, Yan-Rong Li⁴, Jin-Ming Bai⁸, Yong-Jie Chen⁴, Pu Du⁴, Michael Goad⁹,
Bo-Wei Jiang⁴, Sha-Sha Li⁸, Yu-Yang Songsheng⁴, Chan Wang⁷, Ming Xiao⁴, and Zhe Yu⁴

¹ Department of Physics and Astronomy & Institute of Earth and Space Exploration, The University of Western Ontario, 1151 Richmond Street, London, Ontario N6A 3K7, Canada; vkhatu@uwo.ca

² School of Physics and Astronomy, University of St Andrews, North Haugh, St Andrews, KY16 9SS, Scotland, UK

³ Department of Physics & Astronomy, Wayne State University, 666 W Hancock Street, Detroit, MI 48201, USA

⁴ Key Laboratory for Particle Astrophysics, Institute of High Energy Physics, Chinese Academy of Sciences, 19B Yuquan Road, Beijing 100049, People's Republic of China

⁵ Department of Physics and Astronomy, The University of Western Ontario, 1151 Richmond Street, London, Ontario N6A 3K7, Canada

⁶ Department of Physics and Astronomy, York University, 4700 Keele Street, Toronto, Ontario M3J 1P3, Canada

⁷ Physics Department, Nanjing Normal University, Nanjing 210097, People's Republic of China

⁸ Yunnan Observatories, The Chinese Academy of Sciences, Kunming 650011, People's Republic of China

⁹ School of Physics and Astronomy, University of Leicester, Leicester LE1 7RH, UK

Received 2022 December 2; revised 2023 August 30; accepted 2023 September 3; published 2023 November 17

Abstract

We performed a rigorous reverberation-mapping analysis of the broad-line region (BLR) in a highly accreting ($L/L_{\text{Edd}} = 0.74\text{--}3.4$) active galactic nucleus, Markarian 142 (Mrk 142), for the first time using concurrent observations of the inner accretion disk and the BLR to determine a time lag for the H β $\lambda 4861$ emission relative to the ultraviolet (UV) continuum variations. We used continuum data taken with the Niel Gehrels Swift Observatory in the *UVW2* band, and the Las Cumbres Observatory, Dan Zowada Memorial Observatory, and Liverpool Telescope in the *g* band, as part of the broader Mrk 142 multiwavelength monitoring campaign in 2019. We obtained new spectroscopic observations covering the H β broad emission line in the optical from the Gemini North Telescope and the Lijiang 2.4 m Telescope for a total of 102 epochs (over a period of 8 months) contemporaneous to the continuum data. Our primary result states a UV-to-H β time lag of $8.68^{+0.75}_{-0.72}$ days in Mrk 142 obtained from light-curve analysis with a Python-based running optimal average algorithm. We placed our new measurements for Mrk 142 on the optical and UV radius–luminosity relations for NGC 5548 to understand the nature of the continuum driver. The positions of Mrk 142 on the scaling relations suggest that UV is closer to the “true” driving continuum than the optical. Furthermore, we obtain $\log(M/M_{\odot}) = 6.32 \pm 0.29$ assuming UV as the primary driving continuum.

Unified Astronomy Thesaurus concepts: Active galactic nuclei (16); Accretion (14); Spectroscopy (1558)

Supporting material: data behind figure, machine-readable tables

1. Introduction

Accretion onto supermassive black holes through an accretion disk of ionized gas powers active galactic nuclei (AGNs) at the centers of massive galaxies. AGNs accreting at typical rates (a few percent of the Eddington limit) have a geometrically thin but optically thick disk—the “thin-disk” model (Shakura & Sunyaev 1973). However, theoretical models predict a notably different structure for the AGN with high accretion rates significantly above the Eddington limit—super-Eddington AGN (e.g., Abramowicz et al. 1988). The occurrence of such AGNs is likely higher during the peak era of supermassive black hole growth during cosmic noon (redshifts, $z = 1\text{--}3$; Brandt & Alexander 2010; Shen et al. 2020). Understanding the structure of the accretion system in high-Eddington AGNs remains an open issue in accretion physics.

Although models exist for slim-disk systems, observational tests of the structure of the accretion flow in super-Eddington

AGN are rare. At high accretion rates, radiation pressure is expected to dominate, causing the inner disk to inflate vertically—now called a “slim” (rather than thin) disk—with a scale height, $H \leq R$, where R is the disk radius (e.g., Abramowicz et al. 1988). Photons are trapped in the fast-flowing matter, eventually falling into the black hole. Given that not all photons escape, the disks in super-Eddington AGNs are underluminous relative to the accretion rates as compared to thin disks (Jaroszyński et al. 1980). Begelman (2002) proposed an alternative scenario where the “photon-bubble instability” principle can cause the disks in super-Eddington AGNs to become inhomogeneous at scales much smaller than the disk scale height.

Reverberation mapping (RM; Blandford & McKee 1982; Peterson 1993) provides a way to observationally study the slim-disk model and broad-line region (BLR) in super-Eddington AGNs. RM takes advantage of the observed continuum variability of AGNs on many timescales (from several days to weeks and years; e.g., Peterson et al. 1982). The accretion-disk emission illuminates the BLR on larger scales, and sets the ionization structure and thus the location of the gas generating the broad emission lines (e.g., H β). An increase in continuum emission from the accretion disk results in an increase in broad emission-line flux after a time lag set by the sum total of the light travel time between

the continuum-emitting region and the BLR (Peterson 2014), and the recombination timescale, where the latter is much smaller than the former for typical BLR densities (and therefore ignored in the time-lag calculations). RM converts this time lag into a spatial distance, the size of the BLR. Thus, applying RM to high-accretion-rate AGNs gives an observational method to test the structure of the accretion flow and BLR in these systems, and place super-Eddington AGNs on the radius–luminosity (R – L) relationship for AGNs (Kaspi et al. 2005; Bentz et al. 2013).

The Narrow-Line Seyfert 1 (NLS1) class of AGNs are considered to have high accretion rates, and typically display narrow broad emission lines (e.g., the $H\beta$ line has an $\text{FWHM} \lesssim 2000 \text{ km s}^{-1}$) in comparison to other broad-line objects (and broader than the narrow lines seen in type 2 objects), strong Fe II emission lines, and weak [O III] lines (e.g., Osterbrock & Pogge 1987; Boroson & Green 1992; Boller et al. 1996; Véron-Cetty et al. 2001) in their spectra. The Super-Eddington Accreting Massive Black Holes (SEAMBH) campaign has been performing photometric and spectroscopic monitoring over the past 9 yr of high accretion-rate AGNs that display spectral characteristics of NLS1s (e.g., Du et al. 2014, 2015, 2016a, 2016b, 2018; Wang et al. 2014a; Hu et al. 2015; Li et al. 2018, 2021). Du et al. (2016b) showed that the BLRs in super-Eddington AGNs are smaller than those with sub-Eddington accretion rates. In the context of the slim-disk model, the smaller BLR sizes can be explained as a consequence of the increased scale height of the inner accretion disk that shields the BLR from the central ionizing flux (Wang et al. 2014b). $H\beta$, a marker of the hydrogen ionization front in the BLR, can thus exist at smaller radii than in thin accretion-disk systems. Fonseca Alvarez et al. (2020) offered an alternative explanation. In their correlation analysis of the physical and spectral properties of the Sloan Digital Sky Survey (SDSS) RM AGNs, Fonseca Alvarez et al. (2020) found that the R – L offset (defined as the ratio of the measured $H\beta$ time lag to the expected time lag from the best-fit R – L such as that given by Bentz et al. 2013) is positively correlated to the [O III] $\lambda 5008$ to $H\beta$ luminosity ratio, which is often used as a proxy for the number of ionizing photons (e.g., Baldwin et al. 1981). The smaller BLR sizes are therefore likely a result of the changes in the shape of the ultraviolet (UV)/optical spectral energy distribution (SED) of AGNs (Fonseca Alvarez et al. 2020).

As the most promising SEAMBH object—a bright target with an extremely super-Eddington accretion rate ($\dot{M}/\dot{M}_{\text{Edd}} = 250$; Li et al. 2018) and a well-measured $H\beta$ lag—Markarian 142 (Mrk 142 or PG 1022+519, R.A. = $10^{\text{h}}25^{\text{m}}31^{\text{s}}20$, decl. = $+51^{\circ}40'34''.87$, $z = 0.045$) is the target of our study to probe the structure of its BLR. In the 2012 SEAMBH campaign, Mrk 142 was highly variable with a fractional variability amplitude of $F_{\text{var}} = 8.1\%$ at 5100 \AA over a period of 6 months. Its variable nature makes it amenable to RM studies of both accretion-disk structure (from X-ray/UV/optical continuum time-lag studies) and the BLR structure (from continuum-emission line time lags). Accretion-disk RM applies the same principle as BLR RM to the inner and outer regions of the accretion disk to determine its size and temperature profile (Cackett et al. 2007). The more energetic X-ray/UV radiation from the inner disk illuminates the disk at larger radii where the optical photons are generated. Therefore, the lower-energy emission will respond with a positive time lag to changes in the high-energy radiation giving rise to correlated continuum light curves. Mrk 142 has a total $H\beta$ time lag (τ) with respect to the 5100 \AA continuum emission of $7.9_{-1.1}^{+1.2}$ days

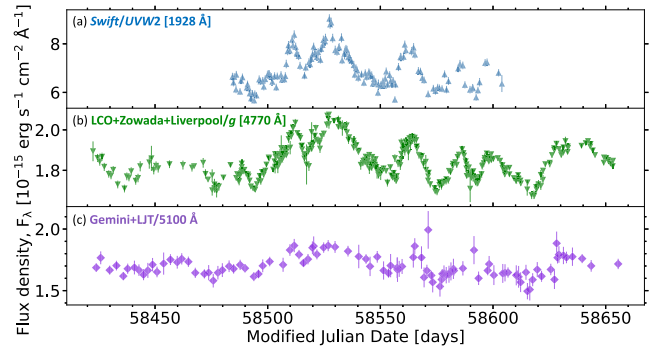


Figure 1. Mrk 142 continuum light curves—UVW2 band with Swift (blue upright triangles, panel (a)) and the g band with LCO, Zowada, and Liverpool (green flipped triangles, panel (b)) from photometric observations; and 5100 \AA (purple diamonds, panel (c)) inter-calibrated from the spectroscopic observations with the Gemini North Telescope (Gemini) and the Lijiang Telescope (LJT). The 5100 \AA inter-calibrated light curve displays the combined spectroscopic coverage over 102 epochs. We performed the inter-calibration with a Python-based running optimal average (PyROA; Donnan et al. 2021) technique (see introduction to PyROA in Section 5.1).

(Du et al. 2015) and a black hole mass of $\log(M_{\bullet}/M_{\odot}) = 6.23_{-0.45}^{+0.26}$ (Li et al. 2018).

In this paper, we present Mrk 142 time-lag measurements from two ground-based, optical spectroscopic RM campaigns of Mrk 142 concurrent with the photometric monitoring of the target with the Neil Gehrels Swift Observatory (Swift) in a UV band; and the Las Cumbres Observatory (LCO), Dan Zowada Memorial Observatory (Zowada), and Liverpool Telescope (Liverpool; Steele et al. 2004) in an optical band. With our joint campaign, we performed, for the first time, simultaneous measurements of the inner accretion disk and BLR size in a super-Eddington AGN. This paper is organized as follows. In Section 2, we provide details of the observations, and in Section 3, we explain the process of data reduction. In Section 4, we describe our spectral modeling followed by light-curve analysis in Section 5. In Section 6, we outline and discuss our results in the context of previous studies. Section 7 provides closing remarks. Throughout this work, we use the standard cosmology with $H_0 = 67 \text{ km s}^{-1} \text{ Mpc}^{-1}$, $\Omega_{\Lambda} = 0.68$, and $\Omega_{\text{M}} = 0.32$ (Planck Collaboration et al. 2014).

2. Observations

We obtained concurrent observations of Mrk 142 with multiple telescopes to perform RM analysis of the accretion disk and BLR simultaneously. Figure 1 shows the continuum light curves of Mrk 142, highlighting the simultaneous coverage with different telescopes.

2.1. Gemini North Telescope

We obtained new observations of Mrk 142 long-slit spectra taken with the Gemini Multi-Object Spectrograph (GMOS; Hook et al. 2004) on the 8.1 m Gemini North Telescope (Gemini) on Maunakea, Hawai'i with 33 epochs from 2019 February 6 through June 1. These spectral observations are concurrent with the Mrk 142 photometric data from the Swift telescope comprising 180 epochs of 1 ks exposures at X-ray, UV, and optical wavelengths from 2019 January 1 through April 30 (P.I.: E. Cackett) as well as with the photometric g -band data from LCO (P.I.: R. Edelson), Zowada (P.I.: E. Cackett), and Liverpool (P.I.: M. Goad); the photometric data

are presented in Cackett et al. (2020). The Swift observations had a twice-daily cadence until March 19, and the cadence was decreased to daily from March 20 onward. We required observations from Gemini in early 2019 with considerable overlap with the Swift campaign to allow, for the first time, simultaneous measurements of the UV-emitting accretion disk and the BLR of a super-Eddington AGN. The cadence of the Gemini observations was set to 1 day. We obtained data for only two, sparsely separated epochs in February during the beginning of the observing period due to weather interruptions. However, observations were more frequent in March and May, and the daily cadence was achieved in the first week of April.

The spectra were taken with the GMOS-North Hamamatsu detector and a single grating, B600 with two different slits, 0"75 (narrow slit) and 5"00 (wide slit), in the two-target acquisition mode, where Mrk 142 and a comparison star were observed in the same slit. The GMOS-North Hamamatsu detector comprises three $\sim 2048 \times 4176$ pixel chips (full detector size of 6278×4176 pixels, mosaicked) arranged in a row with pixel size of 0"0807 with two chip gaps 4"88 wide. The choice of the grating was made to obtain the broad emission line of interest, $H\beta$ $\lambda 4861$, in the spectra. The narrow 0"75 slit was selected to obtain a spectral resolution of ~ 1125 (narrow-slit data) required to study the velocity structure of $H\beta$. Accuracy in spectrophotometric calibration is a key for RM studies, and therefore, we used the wide slit at a resolution of ~ 170 (wide-slit data) to correct for slit losses due to the narrow slit. To satisfy this calibration requirement, Mrk 142 and a comparison star for flux calibration (hereafter, calibration star) were placed simultaneously in the same slit. We achieved this for all observations by fixing the position angle of the slits at $155^\circ 20'$ east of north such that Mrk 142 appeared at the center of the slit. The selected G-type calibration star (R.A. = $10^h 25^m 36^s 37$, decl. = $+51^\circ 38' 52'' 18$, r -band magnitude = 15.9 from the SDSS catalog) has a well-calibrated spectrum and was used for previous LJT campaigns. Flatfield images were taken for every object (science target and calibration star) with the Gemini Facility Calibration Unit (GCAL) in the sequence FLAT–OBJECT–OBJECT–FLAT with both slits. The on-target exposures were 90 s long. We also took daytime arc-lamp spectra with the CuAr lamp, again, for both slits. Binning of 1 in the spectral (X) direction and 2 in the spatial (Y) direction (1×2) was used for all data except for the wide-slit arc-lamp spectra, which used the binning of 1×1 . A summary of the GMOS-North science observations is provided in Table 1. The object spectra from all epochs except the narrow-slit spectra from epoch 30 were assigned a Pass ("P") flag.

2.2. Lijiang Telescope

To complement the short observing period of 33 epochs with Gemini, we incorporated supporting observations of Mrk 142 for our study. We observed Mrk 142 with the Yunnan Faint Object Spectrograph and Camera on the Lijiang 2.4 m Telescope (LJT; Wang et al. 2019) in the two-target acquisition mode with the same calibration star as used for the Gemini observations. We followed the same observing procedure as for previous SEAMBH campaigns (e.g., Du et al. 2014, 2015). We obtained long-slit spectra of the target at 69 epochs from 2018 November 1 through 2019 June 21, contemporaneously with the Swift, LCO+Zowada+Liverpool, and Gemini observing campaigns.

Table 1
Summary of Mrk 142 GMOS Observations from 2019 February to June

Epoch	UT ^a Date (YYYY-MM-DD)	MJD ^b Start Time		Airmass	
		0"75 Slit	5"00 Slit	0"75 Slit	5"00 Slit
1	2019-02-06	58520.412	58520.418	1.275	1.258
		58520.414	58520.420	1.270	1.254
2	2019-02-26	58540.415	58540.421	1.181	1.178
		58540.417	58540.423	1.180	1.177
3	2019-03-03	58545.433	58545.439	1.178	1.181
		58545.435	58545.441	1.178	1.182
4	2019-03-09	58551.430	58551.437	1.187	1.193
		58551.432	58551.438	1.188	1.194
5	2019-03-12	58554.550	58554.557	1.679	1.734
		58554.552	58554.558	1.693	1.750
6	2019-03-15	58557.427	58557.433	1.200	1.209
		58557.428	58557.442	1.202	1.225
7	2019-03-16	58558.355	58558.362	1.189	1.184
		58558.357	58558.363	1.188	1.183
8	2019-03-23	58565.281	58565.287	1.299	1.280
		58565.283	58565.289	1.293	1.276
9	2019-03-26	58568.254	58568.260	1.365	1.341
		58568.256	58568.262	1.359	1.335
10	2019-03-27	58569.410	58569.416	1.225	1.237
		58569.411	58569.418	1.228	1.241
11	2019-03-29	58571.233 ^c	58571.239	1.424	1.394
		58571.235 ^d	58571.241	1.416	1.387
12	2019-03-31	58573.233	58573.239	1.398	1.370
		58573.235	58573.241	1.390	1.364
13	2019-04-03	58576.457	58576.463	1.451	1.486
		58576.459	58576.465	1.460	1.496
14	2019-04-04	58577.234	58577.240	1.350	1.327
		58577.235	58577.241	1.343	1.321
15	2019-04-05	58578.241	58578.248	1.312	1.292
		58578.243	58578.249	1.306	1.287
16	2019-04-06	58579.236	58579.242	1.322	1.302
		58579.237	58579.243	1.317	1.297
17	2019-04-07	58580.461	58580.467	1.543	1.585
		58580.463	58580.469	1.554	1.597
18	2019-04-08	58581.331	58581.337	1.177	1.179
		58581.333	58581.339	1.177	1.180
19	2019-04-09	58582.432	58582.438	1.408	1.439
		58582.434	58582.440	1.416	1.447
20	2019-04-25	58598.274	58598.280	1.175	1.176
		58598.276	58598.282	1.175	1.176
21	2019-04-27	58600.391	58600.397 ^e	1.447	1.481
		58600.392	58600.398	1.456	1.491
22	2019-05-01	58604.338	58604.344 ^e	1.282	1.300
		58604.340	58604.346	1.286	1.305
23	2019-05-02	58605.327	58605.333	1.259	1.275
		58605.329	58605.335	1.263	1.280
24	2019-05-07	58610.317	58610.323	1.267	1.285
		58610.318	58610.324	1.272	1.289
25	2019-05-08	58611.361	58611.367	1.450	1.485
		58611.363 ^c	58611.369 ^e	1.459	1.494
26	2019-05-09	58612.246	58612.253	1.177	1.179
		58612.248	58612.254	1.177	1.180
27	2019-05-12	58615.269	58615.275	1.201	1.209
		58615.270	58615.276	1.203	1.212
28	2019-05-13	58616.320 ^e	58616.326	1.329	1.353
		58616.322	58616.328	1.335	1.359
29	2019-05-24	58627.266	58627.272	1.256	1.272
		58627.267	58627.273	1.260	1.276
30	2019-05-25	58628.242 ^f	58628.248	1.213	1.223
		58628.243 ^f	58628.249	1.216	1.227
31	2019-05-26	58629.251	58629.257	1.235	1.249
		58629.253	58629.259	1.239	1.252

Table 1
(Continued)

Epoch	UT ^a Date (YYYY-MM-DD)	MJD ^b Start Time		Airmass	
		0 ^h 75 Slit	5 ^h 00 Slit	0 ^h 75 Slit	5 ^h 00 Slit
32	2019-05-28	58631.251	58631.257	1.246	1.261
		58631.252	58631.258	1.250	1.265
33	2019-06-01	58635.255	58635.262	1.287	1.307
		58635.257	58635.263	1.292	1.312

Notes. Observations were done with the GMOS-North Hamamatsu detector in the two-target acquisition mode (Mrk 142 and a comparison star in the same slit) positioning the slit at 155°20 east of north, with the B600 grating (covering the broad H β emission line at \sim 4862 Å) and two slits, 0^h75 (narrow slit) and 5^h00 (wide slit). Two exposures were taken with every grating/slit combination, each 90 s long. A data quality flag (DQF) of “P” (passable) or “U” (usable) was assigned to all data at the time of observing. Unless stated otherwise, all science spectra were assigned a DQF of “P.” SpectroPhotometric CALibration Flag (SPCALF) indicates whether the science spectra were calibrated (“1”) or not calibrated (“0”) during spectral reduction (see Section 3.1.4 for more details). SpectroPhotometric CALibration Grade (SPCALG) indicates the grade assigned to the spectrophotometric calibration based on the epoch and exposure of the calibration star spectrum used for calibrating the science spectra (see Section 3.1.4 for more details). All science spectra were assigned an SPCALF of 1 and an SPCALG of “A” unless indicated otherwise.

^a UT: universal Time dates.

^b MJD: Modified Julian Date recorded at the start of the observations for individual exposures.

^c Science spectrum assigned SPCALF (see *Note* below) = 0.

^d Science spectrum calibrated with the narrow-slit standard star spectrum from exposure 1 and hence assigned SPCALG (see *Note* below) = B.

^e Science spectrum likely had a calibration issue and hence was not used for further analysis (see [Appendix](#) for details).

^f Science spectrum assigned DQF (see *Note* below) = U.

Two exposures of 1200 s each were taken for each epoch, with Grism 14 and a long slit with a projected width of 2^h5. The yielded spectra cover a wavelength range of 3800–7200 Å, with a dispersion of 1.8 Å pixel⁻¹. The final instrumental broadening is roughly 695 km s⁻¹ in FWHM. Bias, dome flats, and arc-lamp spectra were taken each night for calibrations, and spectrophotometric standards were observed in several nights of good weather conditions.

Table 2 provides a summary of the overlapping photometric and spectroscopic programs.

3. Spectral Reduction

3.1. Gemini Spectral Reduction

The spectral reduction process for all Gemini epochs included four stages (in the order of appearance below) with the Gemini Image Reduction and Analysis Facility (Gemini IRAF¹⁰) reduction package: (1) baseline calibrations with GCAL flats, 2D arc-lamp spectra, and bias frames; (2) cleaning of 2D spectra followed by the wavelength calibration and extraction of 1D science and calibration-star spectra (in the same slit); (3) preparing 1D spectra for analysis with

PrepSpec (see introduction to PrepSpec in Section 4.1); and (4) flux calibration of the 1D science spectra. For each epoch, we first sorted the data into lists of bias frames, GCAL flats, arc-lamp spectra, and object spectra for both the narrow and the wide slits. We then used the same reduction script with different parameter settings for processing the data taken with the two slits.

3.1.1. Baseline Calibrations

Baseline calibrations comprised creating a masterbias image, generating a dispersion solution with the narrow-slit arc-lamp spectra, and constructing masterflat images with both the narrow- and wide-slit flatfield images. For individual observing nights, we used bias frames with the binning of 1 \times 2 and a full-frame readout from the Gemini Observatory Archive.¹¹ We applied an overscan noise correction to all bias images, for a given night, before combining them into a masterbias image. We then reduced the narrow-slit arc-lamp spectra with bias subtraction turned off and used them to generate 2D dispersion solutions with the task `gswavelength`. Generating dispersion solutions was a two-step process—fitting the 1D wavelength solution in the spectral direction and fitting any distortions in the spatial direction. The reference wavelengths for the arc-lamp spectra were used from the Gemini IRAF package. Because the re-binned, wide-slit arc-lamp spectra—binned from 1 \times 1 to 1 \times 2 to match the binning of the corresponding GCAL flats and object spectra—were unable to provide a nondistorted wide-slit dispersion solution, we used the narrow-slit solution to wavelength calibrate the wide-slit data. For a given epoch, we combined the two GCAL flats (including a quantum efficiency correction for each) taken with the two slits to create a masterflat corrected for the uneven illumination along the GMOS detector in the long-slit mode.

3.1.2. Cleaning, Wavelength Calibration, and Extraction

We corrected the 2D object spectra affected by cosmic-ray hits and performed their wavelength calibration to then extract the 1D science and calibration-star spectra. With the task `gscrcrej`, we first selected a fixed square region surrounding the cosmic-ray affected pixels above a specified threshold and then replaced them with interpolated values from local noise levels. However, this method did not correct for all cosmic rays. We applied an additional correction to the affected pixels that remained uncorrected in the next stage of the reduction process. We applied the derived narrow-slit dispersion solutions to both the narrow- and the wide-slit object spectra.

For a given epoch, we extracted 1D science and calibration-star spectra separately from individual exposures with the task `gsextract`. We selected a considerable swath of background for subtraction from both sides of each trace during the extraction process. The subtraction of bright skylines from the extracted 1D spectra resulted in some sharp spikes in the spectra owing to residual noise. We applied an additional correction to remove the sharp features in the 1D spectra in the next stage of reduction (see Section 3.1.3 for details).

A few of the extracted science and calibration-star spectra showed flat regions (zero flux values) on the shorter-wavelength (or blue) end (\sim 3355 to \sim 4325 Å) that do not match the true shape of the continuum, while some spectra

¹⁰ Gemini IRAF is an external package that makes use of IRAF (a software system used for the reduction and analysis of astronomical data, created and supported by the National Optical Astronomy Observatory in Tucson, Arizona). See more at <https://www.gemini.edu/sciops/data-and-results/processing-software/description>.

¹¹ <https://archive.gemini.edu>

Table 2
Summary of Overlapping Photometric and Spectroscopic Observations

Filter/Line	Observatory	Date Range (MJD ^a)	Number of Epochs	Mean Cadence
UVW2 [1928 Å] ^b	Swift	58484.349–58603.941	149	~twice-daily
g [4770 Å] ^b	LCO, Zowada, Liverpool	58422.973–58653.260	361	2 days
H β λ 4861 ^c	Gemini	58520.414–58635.257	33	~3.6 days
H β λ 4861 ^c	LJT	58423.899–58655.549	69	~3.4 days

Notes.

^a MJD: Modified Julian Date.

^b Photometry.

^c Spectroscopy.

showed bump-like features. The flat regions were a consequence of the slit position angle not aligned along the parallactic angle, whereas the bump-like features likely resulted from the flat-fielding process, where a higher-order spline was used to create the masterflat to appropriately trace detector sensitivity near the chip-gap regions and avoid discontinuities in the calibrated spectra near the chip edges. We corrected the spectra containing flat blue ends or bumpy features individually before attempting flux calibration (see Section 3.1.3 for details).

3.1.3. Additional Corrections to 1D Spectra—Preparing Data for PrepSpec

To prepare the spectra for PrepSpec, it was important that each spectrum had no gaps. Before the flux calibration stage, we trimmed the blue ends of the spectra shorter than ~ 4325 Å in the rest frame because they were very noisy and not required for the purposes of this study. We further processed the 1D spectra for: (1) flat blue ends (due to the slit position angle) or bump-like features (from the flat-fielding process) appearing in some spectra; and (2) spectral regions affected by artifacts from cosmic-ray removal and sky subtraction as well as chip gaps with no flux. This additional processing was important for the initial stage of modeling spectra with PrepSpec, the software tool that corrects spectra for relative calibration differences (see Section 4.1 for details).

We developed a script to correct flat and bump-like regions in the 1D spectra in Python¹² v3.6.5. A spline function fit to a reference spectrum modeled the true shape of the affected region. We then modeled the flux over the affected pixels assuming a Gaussian distribution of data points with standard deviation equal to the measured standard deviation at the same location in the reference spectrum. The reference spectrum used for recovery was typically the spectrum from another exposure taken on the same night (see the Appendix for exceptions).

To correct for spectral regions affected by artifacts and chip gaps, we developed another Python script to replace the regions with affected data points by local median values or interpolated and simulated data. In a given window of affected points: (1) if the number of pixels was < 5 , the algorithm replaced every data point by the median value of a range of 5 pixels on either side of that point with the noise equal to the local median noise; and (2) if the number of pixels was ≥ 5 , the algorithm first linearly interpolated across the affected region and then replaced the interpolated points with simulated data

assuming a Gaussian distribution with a standard deviation equal to twice the noise in the interpolated data. The uncertainties for the corrected pixel regions were assigned to be twice as much as the standard deviation of the unaffected individual pixel values in the region.

We used the wide-slit science and calibration-star spectra to correct for the wavelength-dependent slit losses in the narrow-slit spectra with a PyRAF (IRAF with Python wrapper) script. We employed the IRAF task `curfit` to fit a spline function to the ratios of the narrow-slit to the reference spectra. We used a single reference spectrum: the mean of the bright, wide-slit spectra. Finally, we updated the starting pixel value of the wavelength scale in the FITS file headers of the slitloss corrected spectra to generate the appropriate wavelength grid for the trimmed spectra.

The Python scripts for performing the above corrections to prepare spectra for PrepSpec analysis are publicly available on GitHub.¹³

3.1.4. Flux Calibration

The flux calibration process included two steps—fitting a sensitivity curve of the detector response to the flux standard with `gsstandard`, and applying the sensitivity solution to the science spectra with the task `gscalibrate`. For flux calibration, we used the calibration star captured in the same slit as the science target except for a handful of spectra for which we used the star from another exposure of the same epoch (see the Appendix for details). Accordingly, we assigned a SpectroPhotometric CALibration Flag (SPCALF) of 1 (0) for calibrated (noncalibrated) science spectra (stated in Table 1). Based on the epoch and exposure of the standard star spectrum used for calibration, we further assigned a SpectroPhotometric CALibration Grade (SPCALG; see Table 1) to the science spectra as follows.

1. SPCALG “A”: science spectrum calibrated with the standard star spectrum from the same exposure.
2. SPCALG “B”: science spectrum calibrated with the standard star spectrum from the same epoch but different exposure.

The Appendix outlines special cases of spectral reduction that were treated separately.

¹² Visit <https://www.python.org/> for full documentation on Python.

¹³ Please contact the corresponding author for further details.

3.2. LJT Spectral Reduction

We first reduced the LJT spectra with IRAF, following the standard procedures for bias subtraction, flatfield correction, and wavelength calibration. The spectra of both the target and the calibration star were extracted in a uniform aperture of 8".5. For those nights with good weather conditions, the spectra of the calibration star were flux-calibrated using the spectrophotometric standards. We combined these flux-calibrated spectra to generate a fiducial spectrum of the calibration star. Then, for each exposure, a sensitivity function was obtained by fitting the fiducial spectrum to the extracted spectrum of the comparison star. Finally, we performed flux calibration of the target spectrum (see Li et al. 2021 for more details).

3.3. Comparison between Gemini and LJT Spectra

Gemini spectra from 33 epochs and LJT spectra from 69 epochs provided 102 epochs of Mrk 142 spectral observations overlapping with the Swift and LCO+Zowada+Liverpool photometric campaigns. A mean spectrum allows us to visualize spectral features with a high signal-to-noise ratio (S/N) from the combined observations, while an rms spectrum signifies the variability in the spectral features. Figure 2 displays the mean and rms of the Gemini (top) and LJT (bottom) spectra. The higher-resolution Gemini mean spectrum shows sharper emission-line profiles (H β , [O III], and He I) as compared to the LJT mean. At lower resolution, LJT spectra are affected by instrumental broadening, which results in the narrow emission lines, e.g., [O III], appearing broader than in the Gemini mean. The instrumental broadening effect also blurs the Fe II emission (shaded in faint blue) and the coronal lines (high-ionization forbidden transitions shaded in brown) in the LJT mean spectrum. In contrast to the Gemini mean, the Fe II features at ~ 4925 Å and ~ 5030 Å in the LJT mean appear blended with the H β wings on the longer-wavelength (red) side and [O III] $\lambda 5008$, respectively. The rms of the Gemini spectra shows a noisy region blueward of 4750 Å, likely dominated by calibration noise. It is worth noting, however, that the finer wavelength sampling of the Gemini spectra (owing to the narrow-slit observations) makes that region appear even noisier. On the other hand, the region toward the blue end of the LJT rms spectrum shows clear evidence of variability in the He II $\lambda 4687$ line although it is heavily contaminated with Fe II in the surrounding region. Variability in H β is revealed by both the Gemini and the LJT rms spectra. Although no variability in He I is evident from the Gemini rms, the LJT rms shows a weak signature of variability in broad He I. A very low, broad wave appears from ~ 5250 to ~ 5450 Å and from ~ 5650 to ~ 5950 Å in the LJT rms spectrum, likely resulting from calibration. The GMOS chip-gap region in the Gemini spectrum extends from ~ 5350 to ~ 5410 Å, which also appears as a low bump in the rms spectrum.

4. Spectral Analysis

To measure the H β and He I emission lines in the calibrated spectra, we first corrected any discrepancies in the calibrations of the Gemini and LJT spectra, independently with PrepSpec, and then modeled their spectral features with Sherpa. For PrepSpec modeling of Gemini spectra, we used the spectral region from ~ 4430 to ~ 6300 Å. For LJT spectra, we kept the spectral region from ~ 3390 to ~ 6300 Å.

4.1. PrepSpec Modeling

We independently modeled the 64 narrow-slit Gemini spectra and the 69 LJT spectra with PrepSpec¹⁴ (developer: K. Horne) to correct for any relative deviations in the calibrated wavelength and flux scales. PrepSpec models spectra by fitting the continuum and emission lines with a composite model through an iterative process. We included the following model components for fitting the Mrk 142 spectra: (1) [A]verage spectrum (specified by "A")—mean of the input spectra; (2) [C]ontinuum—variations in the continuum emission from the accretion disk modeled as a polynomial defined by $\log \lambda$ with time-dependent coefficients; (3) [W]avelength jitter—inter-spectra shifts in the wavelength scales; (4) [F]lux jitter—time-dependent photometric corrections to minimize the scatter of narrow emission-line fluxes relative to their median; and (4) [B]road-line variations—variability in the broad emission-line features. Modeling emission lines in PrepSpec takes into account the velocity window half-widths of the broad as well as the narrow lines, whose initial values were set to 3000 km s⁻¹ and 500 km s⁻¹, respectively. We set the broad H β $\lambda 4861$ and He I $\lambda 5877$ as variable lines for Gemini spectra, and H γ $\lambda 4342$, He II $\lambda 4687$, H β , and He I $\lambda 5877$ as variable for LJT spectra. The software uses the IZwicky 1 (IZw 1) template model (Véron-Cetty et al. 2001) to fit Fe II emission in the mean spectrum. PrepSpec is not designed to handle gaps in spectra or extremely large flux values, e.g., from cosmic-ray hits. Therefore, chip gaps and artifacts from cosmic-ray correction or sky subtraction in the Gemini spectra were replaced by median or simulated data (see Section 3.1.3 for details) during spectral reduction.

In the PrepSpec modeling stage, we first corrected the Gemini and LJT spectra for pixel shifts relative to the [O III] $\lambda 5008$ line and then modeled the spectra with a composite model. We observed small pixel shifts (< 6 pixels) while aligning the spectra along the wavelength axis. The model components were jointly fit starting with a single component and then adding components up to the ACWFB composite model for both the Gemini and the LJT spectra. PrepSpec determines the best-fitting model by accessing the Bayesian information criterion and reduced χ^2 (χ^2_ν , where ν stands for degrees of freedom) statistics. The goal of the fitting process is to use the fewest possible parameters to describe the data while penalizing the model for the number of parameters used. A good model yields $\chi^2_\nu \sim 1$. Figure 3 displays the final model (dark blue curve) passing through the black mean spectrum (panel (a)) and the model (dark gray curve) to the residual rms (rmsx) spectrum (panel (b)) for the 64 narrow-slit Gemini spectra. The rms spectrum shows that the spectra are noisier at the bluer end.

Figure 4 shows the final model (panel (a)) along with the residuals (in the units of σ ; panel (b)) in grayscale for the Gemini spectra. The best-fit model yielded a χ^2_ν value of 0.782, which indicates overfitting of the data, possibly indicating inaccurate error bars larger than the scatter in the data. The dark regions in the model highlight the prominent emission-line features of H β $\lambda 4861$ and [O III] $\lambda\lambda 4960, 5008$. The weak fluctuations blueward of ~ 4700 Å indicate more noise in that region as compared to the red end of the spectra. The residuals in grayscale display horizontal wiggles that are strongly evident in some spectra. We noted that the wiggles appear in the spectral regions

¹⁴ Find current version of PrepSpec at <http://star-www.st-andrews.ac.uk/~kdh1/lib/prepspec/prepspec.tar.gz>.

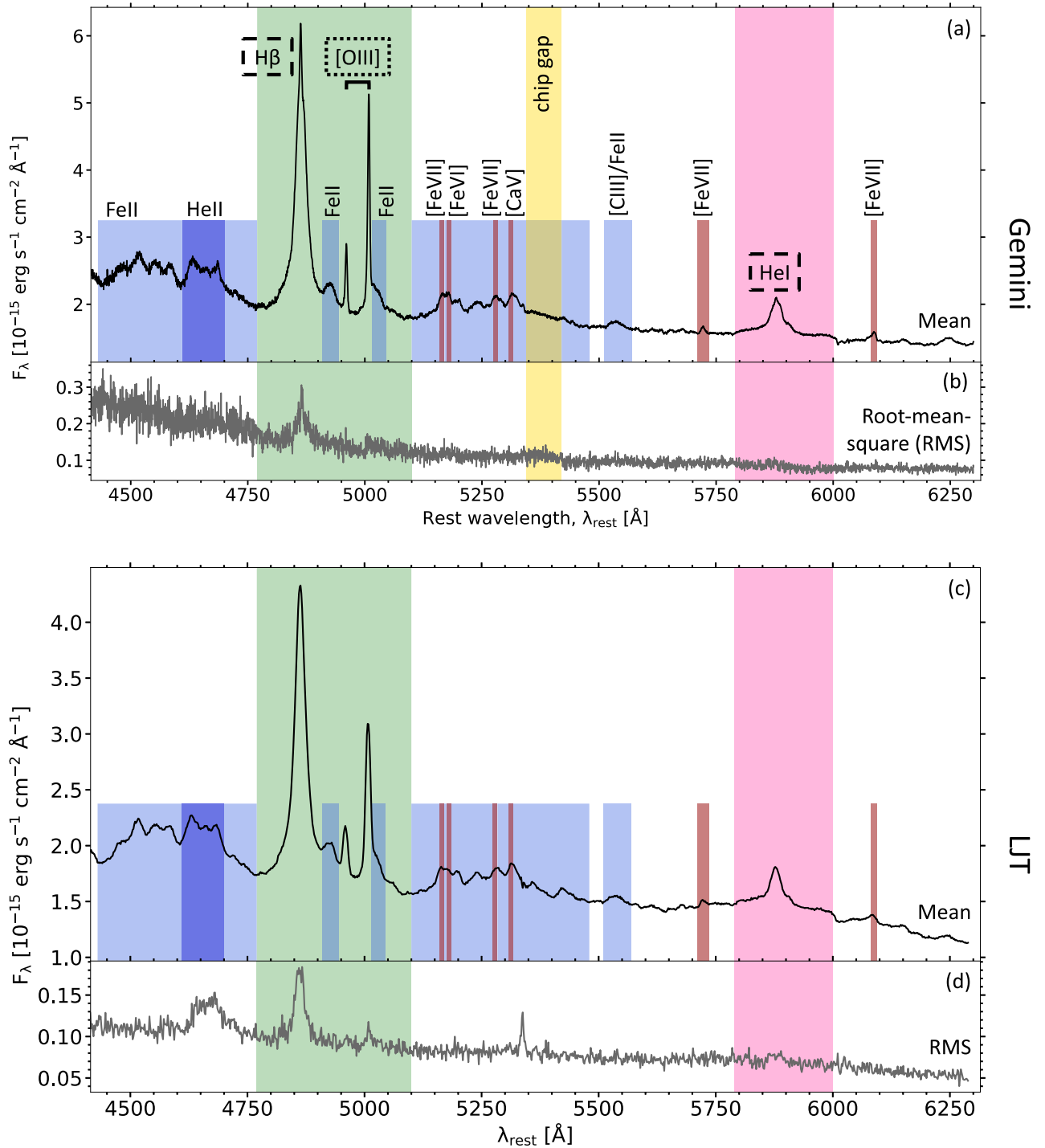


Figure 2. Rest-frame mean (black; panels (a) and (c)) and rms (gray; panels (b) and (d)) of Mrk 142 Gemini (top; velocity resolution of $185.6 \pm 10.2 \text{ km s}^{-1}$) and LJT (bottom; velocity resolution of $695.2 \pm 3.9 \text{ km s}^{-1}$) spectra highlighting the *Regions of Interest*— $\text{H}\beta$ $\lambda 4861$ and $[\text{O III}]$ $\lambda\lambda 4960, 5008$ (region shaded in green), and He I $\lambda 5877$ (region shaded in pink). Labels enclosed in dashed (dotted) boxes indicate broad (narrow) lines. The Gemini mean spectrum shows sharp Fe II features (shaded in faint blue), which appear blended with the red wings of $\text{H}\beta$ and $[\text{O III}]$ $\lambda 5008$ (blue shaded bars) in the LJT mean. Owing to the high signal-to-noise of the Gemini spectra, the peculiar shape of the He I $\lambda 5877$ line is clearly evident. The high-ionization coronal lines (shaded in brown) also appear sharp in contrast to the LJT spectrum, as a result. The LJT rms spectrum shows clear variability in He II (shaded in blue). Both rms spectra indicate variability in the broad $\text{H}\beta$. However, no significant variability is evident in He I over the timescale of Gemini+LJT observations. The yellow-shaded region in the Gemini spectra indicates the GMOS chip gap from ~ 5350 to $\sim 5410 \text{ \AA}$. (The reduced and calibrated Mrk 142 Gemini spectra are available in a machine-readable form.)

(The data used to create this figure are available.)

replaced by simulated data to correct for residual features either from cosmic-ray correction or sky subtraction. The replacement with simulated data may have resulted in a lower performance of

the model in those regions. Another probable reason for the wiggles is the use of a higher-order spline during flat-fielding in the spectral reduction process (refer Section 3.1.3 for details).

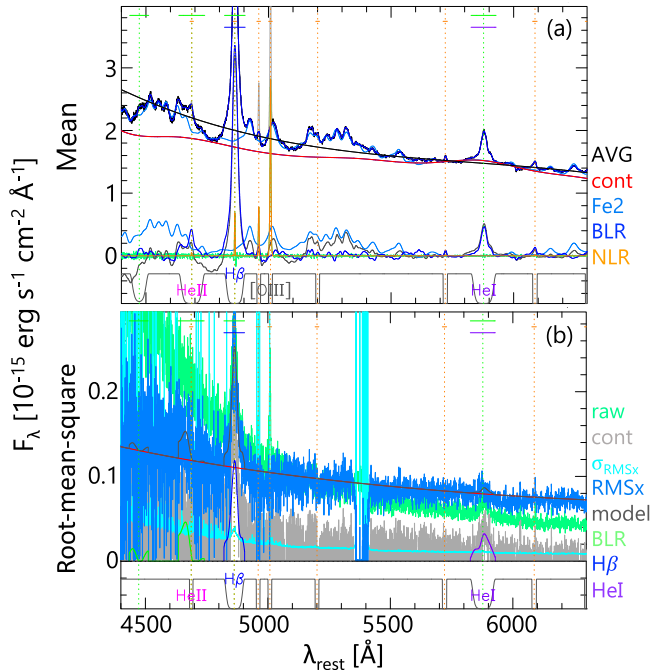
Fe2 30% 577±26 km s⁻¹ BLR 2600 km s⁻¹ NLR 450 km s⁻¹

Figure 3. Mean (panel (a)) and the rms spectra for 64 narrow-slit Mrk 142 Gemini spectra processed through PrepSpec showing model fits with individual components. In panel (a), the composite model (dark blue curve), including the components shown at the bottom of the plot—average spectrum (AVG; black), continuum (cont; red), Fe II (Fe2; faint blue), broad-line region (BLR; dark blue), and narrow-line region (NLR; orange), is overlaid on the mean spectrum (black curve). The broad (narrow) emission lines are indicated with green (orange) dotted vertical lines as well as with green (orange) solid horizontal dashes. The broad lines of H β (blue label) and He I (purple label) are marked with solid horizontal dashes. In panel (b), model (model; dark gray curve) fit to the residual rms spectrum (rmsx; blue curve) includes the components: continuum (cont; red curve) and BLR (green curve at the bottom of the plot). The raw rms spectrum is the upper green curve. The BLR component comprises the broad lines of H β (blue bump around ~ 4862 Å) and He I (purple bump around ~ 5877 Å) shown at the bottom of the plot. The broad He II emission feature at ~ 4687 Å (box-like feature in the model) is contaminated with Fe II and hence difficult to fit given the noise in the region. The deviation in the residual rms spectrum (σ_{rmsx} ; cyan curve) shows large values in the region of the GMOS detector chip gap from ~ 5345 to ~ 5420 Å. In both panels, the active broad-line windows of H β and He I used for PrepSpec modeling are shown in negative-value space.

However, we visually inspected all spectra processed through PrepSpec and observed no anomalous behavior in the regions with wiggles. Therefore, the spectra were considered valid for further analysis.

PrepSpec modeling of LJT spectra yielded nearly even residuals with a χ^2_ν value of 0.791. The region redward of 6300 Å in LJT spectra comprises several blended narrow-line features, which resulted in a suboptimal performance of the PrepSpec model. Therefore, we excluded the red side of the LJT spectra ($\lambda > 6300$ Å) during PrepSpec processing.

4.2. Spectral Modeling in Sherpa

We modeled the continuum and emission lines in the Gemini and LJT spectra in Sherpa¹⁵ (Freeman et al. 2001;

¹⁵ Sherpa is a software application for modeling and fitting astronomical images and spectra. In this work, the Sherpa v4.10.0 application was used within Coronagraphic Imager with Adaptive Optics (CIAO) v4.10.0, the X-ray Data Analysis Software designed by the Chandra X-ray Center. For full documentation of CIAO-Sherpa, see <https://cxc.harvard.edu/sherpa4.14/>.

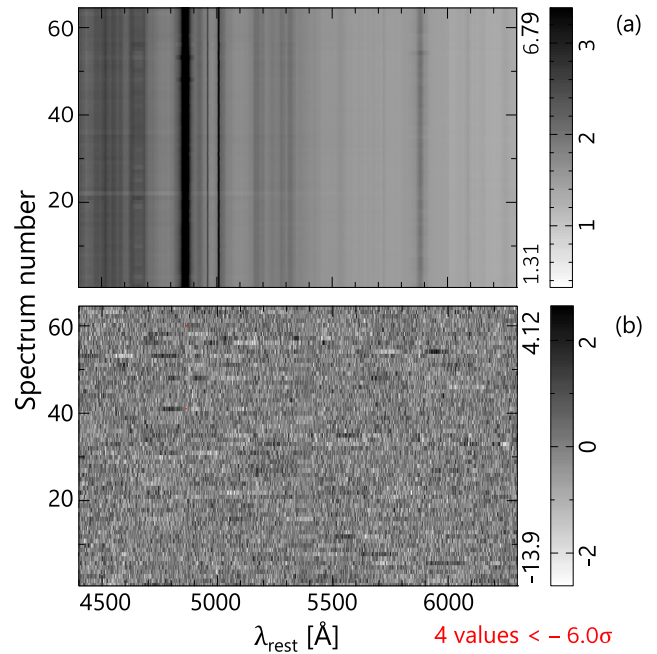
 $\chi^2_\nu = \chi^2 / (250688 - 4317) = 0.782$ 3917 columns \times 64 rows


Figure 4. PrepSpec model including all components (panel (a)) and residuals ($\text{data} - \text{model}$ in units of standard deviation, σ ; panel (b)) with a reduced χ^2 (χ^2_ν) of 0.782 for 64 narrow-slit Mrk 142 spectra. In panel (a), dark regions indicate strong emission lines of H β and [O III], whereas the weaker He I lines and Fe II emission appears as less prominent features. In panel (b), each row represents a single exposure spectrum (where multiple exposures at a given epoch are not yet combined). The horizontal wiggles strongly evident in some spectra are likely the result of either replacing values with simulated data in those regions or using a higher-order function during flat-fielding (see the text for more details). The smeared region from ~ 5345 to ~ 5420 Å is one of the chip gaps of the GMOS detector where simulated data was added during reduction.

Burke et al. 2018) v4.10.0 with a Python wrapper script. We first corrected the Gemini and LJT spectra for Galactic reddening using $E(B - V) = 0.015$ (Schlafly & Finkbeiner 2011). Averaging the two narrow-slit Gemini exposures from every night into a single spectrum per epoch (with exceptions for spectra from epochs 11, 25, and 28, where we only used single exposures) yielded a total of 33 Gemini spectra. Together with the 69 LJT spectra, we modeled a total of 102 Mrk 142 spectra.

We developed a composite model with the goal of performing a clean extraction of the H β and He I emission lines from the Gemini and LJT spectra. We included a power-law fit to the continuum, three Gaussians to model each of the H β , He I, and He II emission lines, and a single Gaussian for each of the [O III] doublet lines. We adopted the IZw 1 template model from Boroson & Green (1992) as a pseudo-continuum to trace the Fe II emission-line features. We also experimented with the Fe II template from Véron-Cetty et al. (2001). However, it failed to suitably trace the sharp Fe II features in Mrk 142. With the Boroson & Green (1992) Fe II template model, the fits yielded lower (χ^2_ν) values than with the Véron-Cetty et al. (2001) template. Following the procedure in Hu et al. (2015), we added single Gaussian profiles for each of the six coronal lines (Fe VII $\lambda 5160$, Fe VI $\lambda 5177$, Ca V $\lambda 5311$, Fe VII $\lambda 5278$, Fe VII $\lambda 5722$, and Fe VII $\lambda 6088$; see Figure 2). In addition, we included the host-galaxy template with 11 Gyr at $z = 0.05$ from the 2013

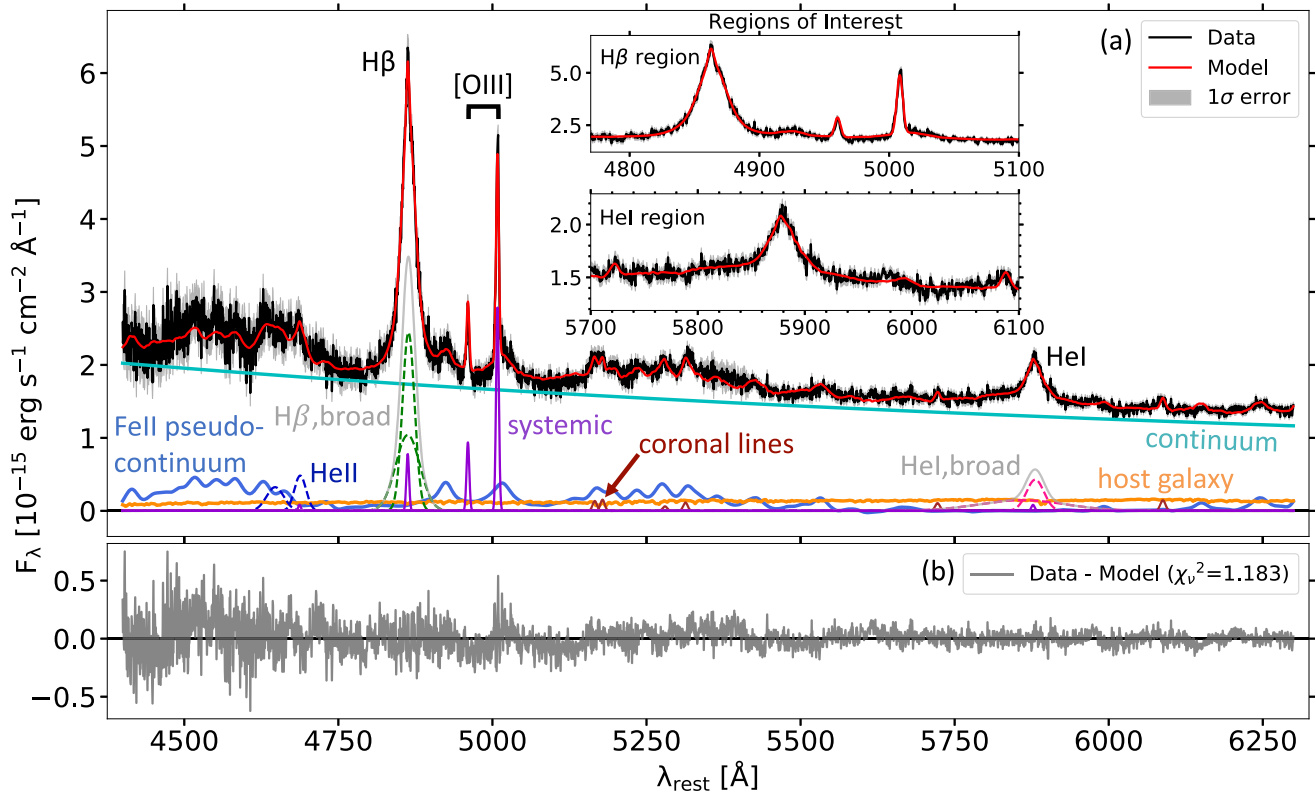


Figure 5. Composite model fit to epoch 24 of the Mrk 142 Gemini data displaying individual components of the model. Panel (a): Composite model (red solid curve) fit to the data (black solid curve) from 4430 to 6300 Å is shown in the main panel, and the H β and He I *Regions of Interest* are shown in the Inset panels. The individual components of the model are displayed at the bottom of the panel: continuum (cyan solid curve); Fe II I Zw 1 template as a pseudo-continuum (faint blue solid curve); host-galaxy template (orange solid curve); He II broad components (blue dashed Gaussians); H β broad components (green dashed Gaussians); He I broad components (pink dashed Gaussians); narrow-line components of H β , He I, and [O III] (purple solid Gaussians); and high-ionization coronal lines (brown solid Gaussians). The total broad H β and He I profiles are also overplotted (gray solid curves). Panel (b): Residuals of the model with $\chi_{\nu}^2 = 1.183$. The model shows larger residuals around the [O III] $\lambda 5008$ line indicating a suboptimal fit in that region. The noisier blue end of the spectrum affects the overall fit in that region, thus resulting in larger residuals compared to the red end of the spectrum.

updated version of Bruzual & Charlot (2003) galaxy templates. The host-galaxy template, affecting the redder part of the spectrum more than the bluer, contributed greatly in producing a good fit to the He I emission-line region. The fit in the H β region was less sensitive to host-galaxy emission. We referred to the Vanden Berk et al. (2001) rest wavelengths for setting the positions of all emission lines.

4.2.1. Gemini Spectral Analysis

Our goal of spectral fitting was to accurately estimate the H β , [O III], and He I profiles in the Gemini spectra. We aimed at finding a robust and flexible set of parameters that fit the structure in the spectra over all epochs. Figure 5 shows the composite model fit to a single-epoch Gemini spectrum.

We describe the fitting process as follows. The Gaussian used for each of the [O III] doublet lines traces the systemic narrow-line emission peaks. While fitting the Gemini spectra, the position, FWHM, and flux of the [O III] $\lambda 5008$ emission line were freed. However, we fixed the position of the [O III] $\lambda 4960$ line relative to the [O III] $\lambda 5008$ line and the flux in the [O III] $\lambda 4960$ line to a factor of 1/3 compared to the [O III] $\lambda 5008$ flux. We chose Gaussians over Lorentzians to appropriately trace the narrower wings of the [O III] lines. We fixed the positions of the narrow components of H β , He I, and He II relative to the position of the [O III] $\lambda 5008$ line, and their widths equal to the [O III] $\lambda 5008$ FWHM. Spectral fitting in

Sherpa takes into account the scaling of the FWHM for a given line relative to the calibrator line, which is the [O III] $\lambda 5008$ line for this work. The position and flux parameters of the two broad components of both H β and He I were freed. The width of only one of the H β Gaussians was allowed to vary while the second Gaussian was fixed at twice the width of the first. On the other hand, the widths of the He I broad components were fixed at factors of 1 and 6 of the FWHM of the flexible, broad H β component. We determined the above FWHM ratios for the broad H β and He I emission lines from the mean spectrum. The insets in Figure 5 show a closer view of the two *Regions of Interest*—H β and He I. A single broad component of He II with position fixed relative to the flexible, broad H β component and width equal to the FWHM of the same component proved insufficient to trace the broader emission around ~ 4650 Å, indicating a plausible blueshifted broad component of He II. Adding another blue-shifted Gaussian 1.5 times the width of the flexible, broad H β component with flux equal to that of the first broad He II component significantly improved the fit in that region. Table 3 lists the emission-line parameters along with their settings as used during spectral fitting.

We followed the Fe II template fitting procedure described in Hu et al. (2015), where the Fe II emission is defined by a convolution of the Boroson & Green (1992) template with a Gaussian. We applied the Gaussian as a 1D point-spread

Table 3
Emission-line Fitting Parameters for Gemini and LJT Spectra

Line	Parameter	Fixed Relative to Line ^a	Ratio Relative to the Fixed Line	
			Gemini	LJT
[O III] λ 5008	Position
	FWHM
	Flux
[O III] λ 4960	Position	[O III] λ 5008	0.990	0.990
	FWHM	[O III] λ 5008	1.000	1.000
	Flux	[O III] λ 5008	0.333	0.333
Narrow H β λ 4861	Position	[O III] λ 5008	0.971	0.971
	FWHM	[O III] λ 5008	1.000	1.000
	Flux	[O III] λ 5008	...	0.293
Narrower broad H β λ 4861	Position
	FWHM
	Flux
Broader broad H β λ 4861	Position
	FWHM	Narrower broad H β λ 4861	2.000	2.500
	Flux
Narrow He I λ 5877	Position	[O III] λ 5008	1.174	1.174
	FWHM	[O III] λ 5008	1.000	1.000
	Flux	[O III] λ 5008	...	0.034
Narrower broad He I λ 5877	Position
	FWHM	Narrower broad H β λ 4861	1.200	1.000
	Flux
Broader broad He I λ 5877	Position
	FWHM	Narrower broad H β λ 4861	6.000	6.000
	Flux
Narrow He II λ 4687	Position	[O III] λ 5008	0.936	0.936
	FWHM	[O III] λ 5008	1.000	1.000
	Flux
Narrower broad He II λ 4687	Position	Narrower broad H β λ 4861	0.964	0.964
	FWHM	Narrower broad H β λ 4861	1.000	1.000
	Flux
Blueshifted broad He II λ 4687	Position	Narrower broad H β λ 4861	0.956	0.956
	FWHM	Narrower broad H β λ 4861	1.500	1.500
	Flux	Narrower broad He II λ 4687	1.000	1.000

Note.

^a Parameter settings with no data indicate that the parameter was kept flexible during spectral fitting.

function with a fixed FWHM, and the amplitude of the convolved Fe II model was set as a flexible parameter while fitting. Although the Fe II model successfully traces the sharp Fe II features in most parts of the spectrum, it performs suboptimally near the Fe II emission at the red wing of the [O III] λ 5008 line, thus resulting in larger residuals in that region. Further, the model overestimates the emission between

the two [O III] lines due to the broader wing of Fe II from the template model.

Modeling individual coronal lines in the spectra considerably improved the fit in the Fe II emission region from \sim 5150 to \sim 5350 Å. In this region, the Fe coronal lines appeared to be slightly redshifted (\leq 0.003) with respect to their rest wavelengths. We set the coronal-line widths to 1.5 times the [O III] λ 5008 line width and their flux values to specific fractions of the [O III] λ 5008 flux, as determined from the fit to the Gemini mean spectrum.

From spectral modeling, we derived, at each epoch, the total FWHM and flux values of the H β , He I, and [O III] lines. We measured the FWHM of the broad and total (including both the broad and the narrow components) H β and He I lines empirically by subtracting all other model components from the spectra including the narrow lines. To calculate the contribution from the broad-line and total (again, including both the broad- and the narrow-line) flux in the H β and He I emission profiles, we simply added the contribution from each of their components. Tables 4–6 provide emission-line measurements for the Gemini spectra from 33 epochs. For epoch 11, the model failed to constrain the broad H β emission as the region blueward of the H β line appeared noisier compared to the other epochs. We therefore excluded epoch 11 from further analysis. Also, due to improper flux calibration at the location of the H β line in epoch 25, the line appeared unusually broader and brighter than at the other epochs. We therefore excluded the spectrum from epoch 25 as well.

4.2.2. LJT Spectral Analysis

We fit the 69 LJT spectra with the same goal of modeling the H β , [O III], and He I lines accurately. Figure 6 shows the fit to a single-epoch LJT spectrum.

We adopted the same model as for the Gemini spectra with small modifications to the ratios of certain fixed parameters. We determined the flux ratios for the coronal lines relative to the [O III] λ 5008 line flux from the fit to the mean LJT spectrum. The width of the fixed broad H β Gaussian was fixed at a factor of 2.5 (instead of 2 for the Gemini spectra). A factor of 2 for this second H β Gaussian in LJT spectra was insufficient to trace the broad wing of H β , which also affected the fit to the blended Fe II feature at \sim 4923 Å. Therefore, a broader H β component was required to generate a good fit in that region. This indicates an interplay between the broad H β and Fe II line emission in the fitting process. Similarly, the [O III] λ 5008 appears to be blended with the Fe II emission feature at its red wing. This is caused by the instrumental broadening in LJT spectra that further resulted in wider [O III] FWHM measurements than typically expected for [O III] in NLS1 objects. To contain the effect of the “broader” [O III] FWHM measurements on the H β and He I line measurements, we fixed the narrow-line flux ratios of H β to [O III] λ 5008 and He I to [O III] λ 5008 from the Gemini spectral measurements (see Table 3). Tables 7–9 provide emission-line measurements for the LJT spectra from 69 epochs.

5. Light-curve Analysis

We used the Mrk 142 Gemini and LJT spectral measurements to generate light curves for the broad H β and He I emission-line profiles. We obtained the total broad-line light curves by integrating the flux under the two broad components

Table 4
[O III] λ 5008 Emission-line Measurements for Gemini Spectra

Epoch	Position _{[O III]λ5008} (Å)	FWHM _{[O III]λ5008} (km s ⁻¹)	F _{[O III]λ5008} (10 ⁻¹⁵ erg s ⁻¹ cm ⁻²)	χ^2_ν ^a
1	5008.21 ± 0.04	313 ± 5	15.7 ± 0.2	1.07
2	5008.19 ± 0.05	318 ± 9	15.8 ± 0.3	1.06
3	5008.12 ± 0.04	325 ± 6	16.1 ± 0.2	1.23
4	5008.19 ± 0.04	303 ± 9	15.7 ± 0.3	1.21
5	5008.18 ± 0.05	320 ± 5	16.2 ± 0.3	0.99
6	5008.20 ± 0.04	325 ± 3	16.1 ± 0.2	1.08
7	5008.23 ± 0.03	311 ± 4	15.5 ± 0.2	1.18
8	5008.15 ± 0.04	322 ± 5	16.1 ± 0.2	1.22
9	5008.15 ± 0.05	336 ± 7	16.1 ± 0.3	0.97
10	5008.11 ± 0.04	326 ± 5	16.0 ± 0.3	1.04
11	5008.11 ± 0.07	317 ± 9	15.6 ± 0.5	0.99
12	5008.16 ± 0.06	333 ± 10	16.3 ± 0.4	1.08
13	5008.19 ± 0.04	304 ± 6	15.6 ± 0.3	1.12
14	5008.16 ± 0.04	317 ± 5	15.8 ± 0.2	1.24
15	5008.20 ± 0.04	319 ± 4	15.9 ± 0.2	1.20
16	5008.19 ± 0.04	311 ± 5	15.6 ± 0.2	1.26
17	5008.22 ± 0.04	315 ± 4	16.0 ± 0.2	1.27
18	5008.14 ± 0.04	338 ± 6	16.1 ± 0.2	1.33
19	5008.22 ± 0.04	312 ± 2	15.8 ± 0.2	1.10
20	5008.21 ± 0.03	292 ± 6	15.5 ± 0.2	1.17
21	5008.23 ± 0.04	313 ± 6	16.0 ± 0.2	1.28
22	5008.18 ± 0.03	308 ± 6	15.8 ± 0.2	1.21
23	5008.20 ± 0.03	304 ± 4	15.6 ± 0.2	1.24
24	5008.15 ± 0.04	320 ± 3	15.8 ± 0.2	1.18
25	5008.20 ± 0.05	307 ± 5	15.9 ± 0.3	1.11
26	5008.20 ± 0.05	310 ± 7	15.9 ± 0.3	1.19
27	5008.21 ± 0.04	302 ± 5	15.5 ± 0.2	1.24
28	5008.34 ± 0.05	301 ± 2	15.3 ± 0.3	1.07
29	5008.18 ± 0.04	323 ± 7	16.1 ± 0.3	1.19
30	5008.24 ± 0.04	321 ± 4	15.9 ± 0.2	1.35
31	5008.27 ± 0.03	306 ± 5	15.7 ± 0.2	1.16
32	5008.25 ± 0.04	321 ± 6	16.0 ± 0.3	1.10
33	5008.22 ± 0.05	328 ± 4	16.4 ± 0.2	1.05

Note.

^a Reduced χ^2 , $\chi^2_\nu = \chi^2/\nu$, where ν indicates 3897 degrees of freedom, gives the model statistic for individual epochs.

(This table is available in machine-readable form.)

(see green dashed Gaussians for H β and pink dashed Gaussians for He I in Figures 5 and 6) for the two emission lines.

We scaled the broad H β light curve from Gemini to the broad H β light curve from LJT to generate an inter-calibrated light curve. The H β light curves from Gemini and LJT were offset by $\sim 25\%$ from each other although they displayed similar fluctuations in their patterns. The offset can be attributed to various factors—different seeing conditions at Gemini and LJT or even the difference in the calibrations from the two telescopes. Because we are interested in measuring a time shift in the pattern with reference to the continuum variations, scaling and combining the light curves is valid for our purpose. Figure 7 shows the scaled broad H β light curve plotted with the original Gemini and LJT light curves. We then inter-calibrated the original H β light curve from LJT and the scaled H β light curve from Gemini with PyROA (see Section 5.1) to use the combined light curve to determine the time lag between the continuum and emission-line variability.

5.1. Cross-correlation Time Lags

We cross-correlated the broad H β Gemini+LJT inter-calibrated light curve with the UVW2 light curve from Swift

to measure the reverberation lag of the BLR response to the continuum variability from the accretion disk, which is at smaller size scales than the BLR. Following Cackett et al. (2020), we chose the UVW2 because we aim to measure the response of H β line-emitting gas to the UV continuum and the UVW2 was the shortest wavelength available from the photometric monitoring of Mrk 142. During cross-correlation, we also included the LCO+Zowada+Liverpool/g, the inter-calibrated 5100 Å continuum from Gemini and LJT data, and the LJT broad H β light curves to use maximum available information for a reliable measurement of the variability pattern.

We employed Python-based running optimal average (PyROA; Donnan et al. 2021) to calculate cross-correlation time lags. PyROA¹⁶ uses a running optimal average (ROA) calculated with a window function (defined by a Gaussian by default) of a certain width to estimate light-curve behavior while fitting all input light curves simultaneously. The width of the window function controls the flexibility of the model in deriving the driving light curve—a narrower window function

¹⁶ See PyROA code and documentation at <https://github.com/FergusDonnan/PyROA>.

Table 5
 $H\beta$ $\lambda 4861$ Emission-line Measurements for Gemini Spectra

Epoch	FWHM $_{H\beta,b}$ (km s $^{-1}$)	$F_{H\beta,b}$ (10^{-15} erg s $^{-1}$ cm $^{-2}$)	FWHM $_{H\beta,n}$ (km s $^{-1}$)	$F_{H\beta,n}$ (10^{-15} erg s $^{-1}$ cm $^{-2}$)	FWHM $_{H\beta,t}$ (km s $^{-1}$)	$F_{H\beta,t}$ (10^{-15} erg s $^{-1}$ cm $^{-2}$)
1	1777 \pm 72	112.2 \pm 2.4	312 \pm 5	5.3 \pm 0.4	1445 \pm 52	117.5 \pm 2.4
2	1681 \pm 109	106.3 \pm 4.3	317 \pm 8	5.5 \pm 0.6	1324 \pm 83	111.8 \pm 4.3
3	1703 \pm 69	115.8 \pm 5.1	325 \pm 5	5.1 \pm 0.4	1412 \pm 73	120.9 \pm 5.1
4	1745 \pm 83	110.5 \pm 2.7	303 \pm 9	4.5 \pm 0.4	1478 \pm 67	115.0 \pm 2.7
5	1555 \pm 80	107.5 \pm 3.4	319 \pm 4	3.1 \pm 0.6	1466 \pm 96	110.6 \pm 3.4
6	1830 \pm 77	109.3 \pm 3.7	324 \pm 3	5.1 \pm 0.5	1524 \pm 80	114.4 \pm 3.7
7	1797 \pm 69	112.2 \pm 2.2	310 \pm 3	4.5 \pm 0.4	1525 \pm 56	116.7 \pm 2.2
8	1697 \pm 62	106.5 \pm 2.3	321 \pm 4	3.5 \pm 0.4	1447 \pm 62	110.0 \pm 2.4
9	1499 \pm 83	100.2 \pm 3.1	336 \pm 6	5.1 \pm 0.6	1379 \pm 58	105.4 \pm 3.2
10	1593 \pm 77	103.4 \pm 2.7	326 \pm 4	5.0 \pm 0.4	1328 \pm 55	108.4 \pm 2.8
11 ^a	1637 \pm 132	104.3 \pm 3.3	317 \pm 9	5.7 \pm 0.8	1235 \pm 165	110.1 \pm 3.4
12	1732 \pm 120	101.5 \pm 5.8	332 \pm 10	5.9 \pm 0.7	1322 \pm 81	107.3 \pm 5.8
13	1628 \pm 88	101.3 \pm 2.5	303 \pm 6	3.7 \pm 0.5	1354 \pm 77	105.0 \pm 2.5
14	1707 \pm 69	109.1 \pm 2.6	316 \pm 5	4.2 \pm 0.4	1384 \pm 56	113.3 \pm 2.7
15	1672 \pm 104	108.8 \pm 2.7	319 \pm 3	4.9 \pm 0.4	1341 \pm 30	113.7 \pm 2.7
16	1780 \pm 76	103.2 \pm 2.3	311 \pm 5	4.4 \pm 0.4	1412 \pm 73	107.6 \pm 2.3
17	1623 \pm 65	108.4 \pm 3.0	315 \pm 4	3.8 \pm 0.4	1402 \pm 60	112.2 \pm 3.0
18	1712 \pm 72	105.6 \pm 2.4	337 \pm 5	4.6 \pm 0.5	1477 \pm 64	110.2 \pm 2.4
19	1579 \pm 91	106.1 \pm 4.2	311 \pm 1	6.1 \pm 0.5	1348 \pm 64	112.2 \pm 4.2
20	1558 \pm 62	115.2 \pm 2.1	291 \pm 5	3.4 \pm 0.4	1473 \pm 42	118.7 \pm 2.1
21	1604 \pm 43	112.6 \pm 2.1	312 \pm 5	3.6 \pm 0.4	1446 \pm 71	116.2 \pm 2.1
22	1698 \pm 62	109.3 \pm 2.8	307 \pm 5	4.4 \pm 0.4	1442 \pm 55	113.7 \pm 2.8
23	1590 \pm 57	108.3 \pm 2.1	304 \pm 3	3.7 \pm 0.4	1416 \pm 52	112.0 \pm 2.2
24	1668 \pm 77	110.9 \pm 2.7	319 \pm 3	4.3 \pm 0.5	1391 \pm 54	115.2 \pm 2.7
25 ^b	1672 \pm 73	140.4 \pm 3.6	307 \pm 5	5.9 \pm 0.7	1603 \pm 83	146.3 \pm 3.7
26	1655 \pm 95	107.0 \pm 2.6	309 \pm 7	4.9 \pm 0.4	1297 \pm 50	111.9 \pm 2.6
27	1649 \pm 48	103.4 \pm 3.9	301 \pm 5	4.6 \pm 0.4	1356 \pm 59	108.0 \pm 3.9
28	1678 \pm 96	102.6 \pm 3.2	300 \pm 2	3.9 \pm 0.6	1459 \pm 148	106.5 \pm 3.3
29	1713 \pm 76	94.9 \pm 3.1	322 \pm 7	4.3 \pm 0.4	1410 \pm 66	99.2 \pm 3.1
30	1754 \pm 96	102.7 \pm 3.7	321 \pm 4	5.5 \pm 0.5	1395 \pm 92	108.2 \pm 3.8
31	1816 \pm 81	109.4 \pm 4.3	306 \pm 5	6.1 \pm 0.4	1489 \pm 96	115.5 \pm 4.3
32	1682 \pm 79	109.6 \pm 2.3	321 \pm 5	4.9 \pm 0.4	1423 \pm 47	114.5 \pm 2.4
33	1699 \pm 58	110.0 \pm 5.0	328 \pm 4	3.8 \pm 0.5	1515 \pm 78	113.8 \pm 5.0

Notes. The second and the third columns providing the FWHM and flux values, respectively, for the broad (“*b*”) $H\beta$ component include contributions from both the broad Gaussians defined for the line. The FWHM of the narrow (“*n*”) $H\beta$ is equal to the FWHM of the [O III] $\lambda 5008$ (see Table 4, third column). The total (“*t*”) FWHM and flux include contributions from both the broad and the narrow components ($t = b + n$).

^a Because the noisy region blueward of the $H\beta$ emission line was unable to well constrain the broad, blue wing of $H\beta$, this epoch was excluded from further analysis.

^b Due to a calibration issue at the location of the $H\beta$ emission line, the $H\beta$ profile appeared unusually broader and brighter than in other spectra. Therefore, this epoch was excluded from further analysis.

(This table is available in machine-readable form.)

traces the fluctuating pattern of a highly variable light curve more appropriately than a wider window, which behaves more rigidly. The code uses priors to initiate the modeling process, and the performance of the model is evaluated using the Bayesian information criterion. PyROA offers a robust treatment for outliers with an extra variance parameter and a standard deviation threshold. The extra variance adds in quadrature to the nominal uncertainties of the input light curves, and the threshold set by the user allows for further inflation of the uncertainties to mitigate the influence of large outliers. Figure 8 shows the cross-correlation results with reference to the Swift/*UVW2* band.

In addition to the $H\beta$ time lag for the Gemini+LJT inter-calibrated light curve (8.68 $^{+0.75}_{-0.72}$ days), PyROA provided lag measurements for other input light curves (0.73 $^{+0.10}_{-0.10}$ days for LCO+Zowada+Liverpool/*g*, 0.79 $^{+0.27}_{-0.29}$ days for Gemini+LJT/5100 Å, and 8.14 $^{+0.82}_{-0.80}$ days for LJT/ $H\beta$) with reference to the Swift/*UVW2* band. With respect to the shorter-wavelength *UVW2* emission, we expect to measure positive lags for the

longer-wavelength emission in the *g* band, at 5100 Å, and for the $H\beta$ emission line. We thus modeled the distribution of time lags as a log-Gaussian function that imposes positive lags with reference to *UVW2*, whose lag is fixed at 0.00 day (see Figure 8). In addition to measuring the time shift in the light-curve pattern, the width of the Log-Gaussian model also accounts for the amount of blurring applied to the reference light curve (here, *UVW2*) to match the response in the echo light curves. This becomes important for BLR RM, where the emission-line variations, emerging farther away from the central engine and from a more spatially extended structure (size scale ~ 1 pc) than the accretion disk, are smoother compared to the continuum variations closer to the center. In PyROA, the width of the time-lag distribution quantifies the blurring determined for each of the echo light curves: 0.28 $^{+0.19}_{-0.18}$ days for LCO+Zowada+Liverpool/*g*, 0.88 $^{+0.62}_{-0.48}$ days for Gemini+LJT/5100 Å, 4.88 $^{+1.16}_{-0.90}$ days for LJT/ $H\beta$, and 5.47 $^{+1.06}_{-0.89}$ days for Gemini+LJT/ $H\beta$. We also performed light-curve analysis with the interpolated cross-correlation

Table 6
He I $\lambda 5877$ Emission-line Measurements for Gemini Spectra

Epoch	FWHM _{He I,<i>b</i>} (km s ⁻¹)	$F_{\text{He I},b}$ (10 ⁻¹⁵ erg s ⁻¹ cm ⁻²)	FWHM _{He I,<i>n</i>} (km s ⁻¹)	$F_{\text{He I},n}$ (10 ⁻¹⁵ erg s ⁻¹ cm ⁻²)	FWHM _{He I,<i>t</i>} (km s ⁻¹)	$F_{\text{He I},t}$ (10 ⁻¹⁵ erg s ⁻¹ cm ⁻²)
1	47 ± 37	34.4 ± 0.8	312 ± 5	0.7 ± 0.1	47 ± 95	35.1 ± 0.8
2	53 ± 37	33.4 ± 1.0	317 ± 8	0.6 ± 0.2	53 ± 36	34.0 ± 1.0
3	90 ± 44	41.3 ± 0.9	325 ± 5	0.7 ± 0.1	90 ± 41	42.0 ± 0.9
4	36 ± 25	36.0 ± 0.9	303 ± 9	0.8 ± 0.1	36 ± 20	36.8 ± 0.9
5	335 ± 70	35.2 ± 1.1	319 ± 4	0.3 ± 0.2	335 ± 71	35.5 ± 1.1
6	46 ± 36	35.1 ± 0.9	324 ± 3	0.6 ± 0.1	46 ± 35	35.7 ± 0.9
7	136 ± 170	39.7 ± 0.8	310 ± 3	0.6 ± 0.1	1962 ± 312	40.3 ± 0.8
8	49 ± 65	39.1 ± 0.7	321 ± 4	0.5 ± 0.1	49 ± 59	39.6 ± 0.7
9	34 ± 43	33.1 ± 0.9	336 ± 6	0.7 ± 0.2	34 ± 46	33.7 ± 0.9
10	92 ± 53	36.3 ± 0.8	326 ± 4	0.7 ± 0.2	92 ± 52	37.0 ± 0.8
11 ^a	153 ± 39	36.6 ± 1.4	317 ± 9	0.4 ± 0.2	153 ± 38	37.1 ± 1.4
12	92 ± 51	31.4 ± 1.3	332 ± 10	0.5 ± 0.2	92 ± 52	32.0 ± 1.3
13	1419 ± 90	35.9 ± 0.9	303 ± 6	0.0 ± 0.2	1419 ± 108	35.9 ± 0.9
14	83 ± 51	41.0 ± 0.8	316 ± 5	0.8 ± 0.1	83 ± 55	41.8 ± 0.8
15	66 ± 41	38.4 ± 0.8	319 ± 3	0.5 ± 0.1	66 ± 41	38.9 ± 0.8
16	152 ± 225	38.8 ± 0.8	311 ± 5	0.6 ± 0.1	1758 ± 497	39.4 ± 0.8
17	1825 ± 303	38.8 ± 0.9	315 ± 4	0.3 ± 0.1	1528 ± 415	39.1 ± 0.9
18	37 ± 32	37.2 ± 0.8	337 ± 5	0.4 ± 0.1	37 ± 181	37.6 ± 0.9
19	1828 ± 42	35.4 ± 0.9	311 ± 1	0.7 ± 0.1	1806 ± 41	36.1 ± 0.9
20	1862 ± 357	42.0 ± 0.7	291 ± 5	0.4 ± 0.1	1829 ± 631	42.4 ± 0.7
21	1798 ± 399	38.4 ± 0.8	312 ± 5	0.9 ± 0.1	1651 ± 647	39.3 ± 0.8
22	1870 ± 654	41.9 ± 0.8	307 ± 5	0.4 ± 0.1	1870 ± 682	42.2 ± 0.8
23	38 ± 189	40.2 ± 0.8	304 ± 3	0.5 ± 0.1	1873 ± 336	40.7 ± 0.8
24	54 ± 84	41.1 ± 0.9	319 ± 3	0.5 ± 0.1	54 ± 132	41.7 ± 0.9
25 ^b	137 ± 43	38.3 ± 1.3	307 ± 5	0.6 ± 0.2	137 ± 45	38.9 ± 1.3
26	61 ± 53	36.9 ± 0.8	309 ± 7	0.5 ± 0.1	61 ± 110	37.4 ± 0.8
27	114 ± 180	38.7 ± 0.9	301 ± 5	0.5 ± 0.1	1935 ± 389	39.3 ± 0.9
28	81 ± 60	55.6 ± 1.1	300 ± 2	0.1 ± 0.2	81 ± 52	55.7 ± 1.1
29	181 ± 100	36.0 ± 0.8	322 ± 7	0.4 ± 0.1	181 ± 96	36.4 ± 0.8
30	34 ± 86	40.0 ± 1.0	321 ± 4	0.5 ± 0.1	34 ± 125	40.5 ± 1.0
31	66 ± 268	44.6 ± 0.9	306 ± 5	0.9 ± 0.1	66 ± 627	45.5 ± 0.9
32	294 ± 50	41.2 ± 0.9	321 ± 5	0.9 ± 0.1	1631 ± 160	42.1 ± 0.9
33	1537 ± 161	35.3 ± 0.9	328 ± 4	0.3 ± 0.1	1528 ± 267	35.6 ± 0.9

Notes. The second and the third columns providing the FWHM and flux values, respectively, for the broad (“*b*”) He I component include contributions from both the broad Gaussians defined for the line. The FWHM of the narrow (“*n*”) He I is equal to the FWHM of the [O III] $\lambda 5008$ (see Table 4, third column). The total (“*t*”) FWHM and flux include contributions from both the broad and the narrow components ($t = b + n$).

^a Excluded from further analysis. See corresponding note in Table 5.

^b Excluded from further analysis. See corresponding note in Table 5.

(This table is available in machine-readable form.)

function (ICCF; Gaskell & Sparke 1986; Gaskell & Peterson 1987) and Just Another Vehicle for Estimating Lags In Nuclei (JAVELIN; Zu et al. 2011, 2013, using a top-hat time-lag distribution function) for comparison with the PyROA results. Table 10 displays the time-lag measurements with all three methods.

5.2. He I Light Curves

The peculiar, asymmetrical shape of the He I line—narrow-line emission and a broad, asymmetrical component (modeled by a Gaussian six times the width of the broad H β line in our spectra fitting procedure)—is clearly evident in the high-S/N Gemini mean spectrum. The asymmetry in the broad component due to the stronger blueshifted emission feature likely indicates a wind component in the BLR. However, the cause of such a disk-wind component is not clear. Leighly (2004) performed CLOUDY simulations to model 10 high- and low-ionization emission lines observed in NLS1s. She suggested that the blueshifted emission evident in the high-ionization lines in NLS1s arises from a wind moving toward us.

Interestingly, the plausible broad, blueshifted component for He II in the spectral model may also be a result of such a wind emission. Further analysis of the He II line is needed to draw firm inferences in this regard. In addition to the blueshifted wind, Leighly (2004) found that the high-ionization Ly α was dominated by emission in the accretion-disk atmosphere or at the low-velocity base of the broad-line wind. The very broad, flattened emission feature in He I may be indicative of a disk-wind feature as noted for Ly α . Furthermore, Leighly (2004) derived a small covering fraction for the BLR. She argued that in an object with a small black hole mass, as in the case of Mrk 142 ($M_* = 3.89 \times 10^6 M_\odot$ ¹⁷), a small covering fraction can result from an emission-line region closer to the plane of the disk. Li et al. (2018) performed velocity-resolved RM of Mrk 142, where the authors concluded that the two-zone BLR model (Wang et al. 2014b) best fit the Mrk 142 BLR with an opening angle (θ) of 10°–30° (representing a disk-like BLR). Estimating the covering fraction from the opening angle as

¹⁷ $1 M_\odot = 1$ Solar mass.

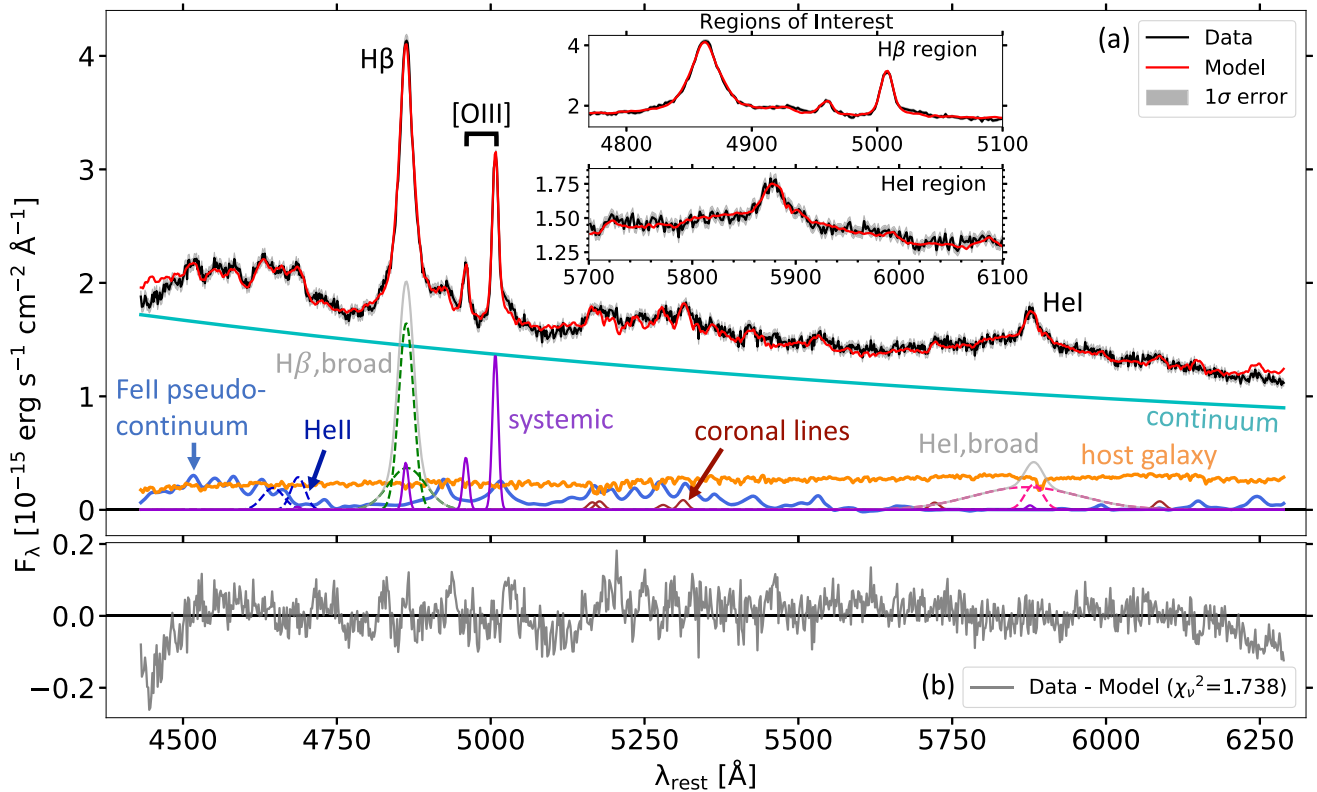


Figure 6. Composite model fit to epoch 24 of the Mrk 142 LJT data displaying individual components of the model. See caption of Figure 5 for a description of the individual model components in Panel (a). The red side of the broad H β emission line shows contamination with the Fe II emission at ~ 4923 Å. Similarly, the [O III] $\lambda 5008$ line shows considerable blending with the Fe II feature in its red wing, thus affecting a reliable measurement of the [O III] $\lambda 5008$ line. Panel (b) shows the residuals of the model with $\chi_r^2 = 1.711$. The smaller residuals indicate an overall good fit to the spectrum. The model performance drops significantly at both ends of the spectrum although it does not impact measurements in the *Regions of Interest*.

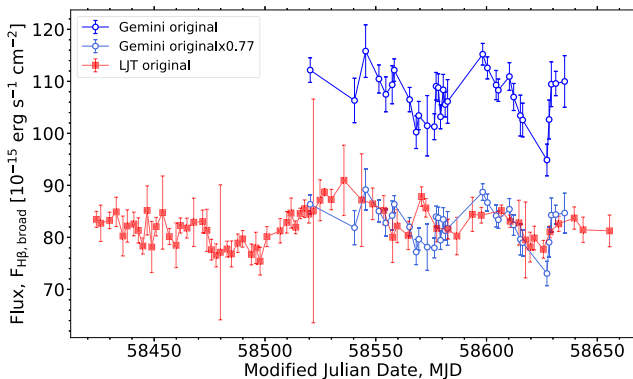


Figure 7. Broad H β light curve from Gemini (dark blue open circles) scaled down (faint blue open circles) to the broad H β light curve from LJT (red solid squares). The scaling factor of 0.77 was determined such that the Gemini data points are distributed evenly above and below the LJT light curve. The two light curves show similar behavior except at Modified Julian Date ~ 58540 , where the LJT light curve increases in flux, while the Gemini light curve appears fainter.

$\theta/90^\circ$ yields a value of 0.1–0.3 for the covering fraction; however, these small values do not confirm the presence of a disk wind in Mrk 142. To understand the components that form the atypical Mrk 142 BLR system or the kind of BLR geometry in a super-Eddington that can show a broad, blueshifted emission feature similar to the He I line feature, we would need further investigation of BLR models and data for super-Eddington AGNs.

Although the LJT rms spectrum of Mrk 142 shows a weak variable feature for He I, the variability is not usefully quantifiable given the timescale and S/N of our current Gemini+LJT spectroscopic campaigns. Figure 9 displays the individual and total broad-line components of He I emission from both the Gemini and the LJT observations. The offset observed in the narrower broad component is similar to that observed in the broad H β , where the light curve from Gemini appears at higher flux values than the LJT light curve. Interestingly, the broader broad component is brighter in LJT than in Gemini likely resulting from the blueshifted disk-wind component broadened due to the wider slit used for LJT data.

6. Results and Discussion

We present the first results on the lag of the broad H β line with respect to the UV continuum in Mrk 142 from optical spectroscopic observations from Gemini+LJT with simultaneous monitoring in the photometric Swift/*UVW2* and LCO +Zowada+Liverpool/*g* bands.

We applied a spectral model with same number of components but different parameter settings to the Gemini and LJT spectra to derive H β and He I light curves. We noted that a profile composed of one narrow + two broad Gaussians sufficiently traced both the H β and the He I lines, where the widths and positions of the narrow components were tied to those of the [O III] $\lambda 5008$ line. The use of Gaussians for fitting broad lines such as H β in our data does not comply with the Wang et al. (2014b) line-profile predictions for a super-

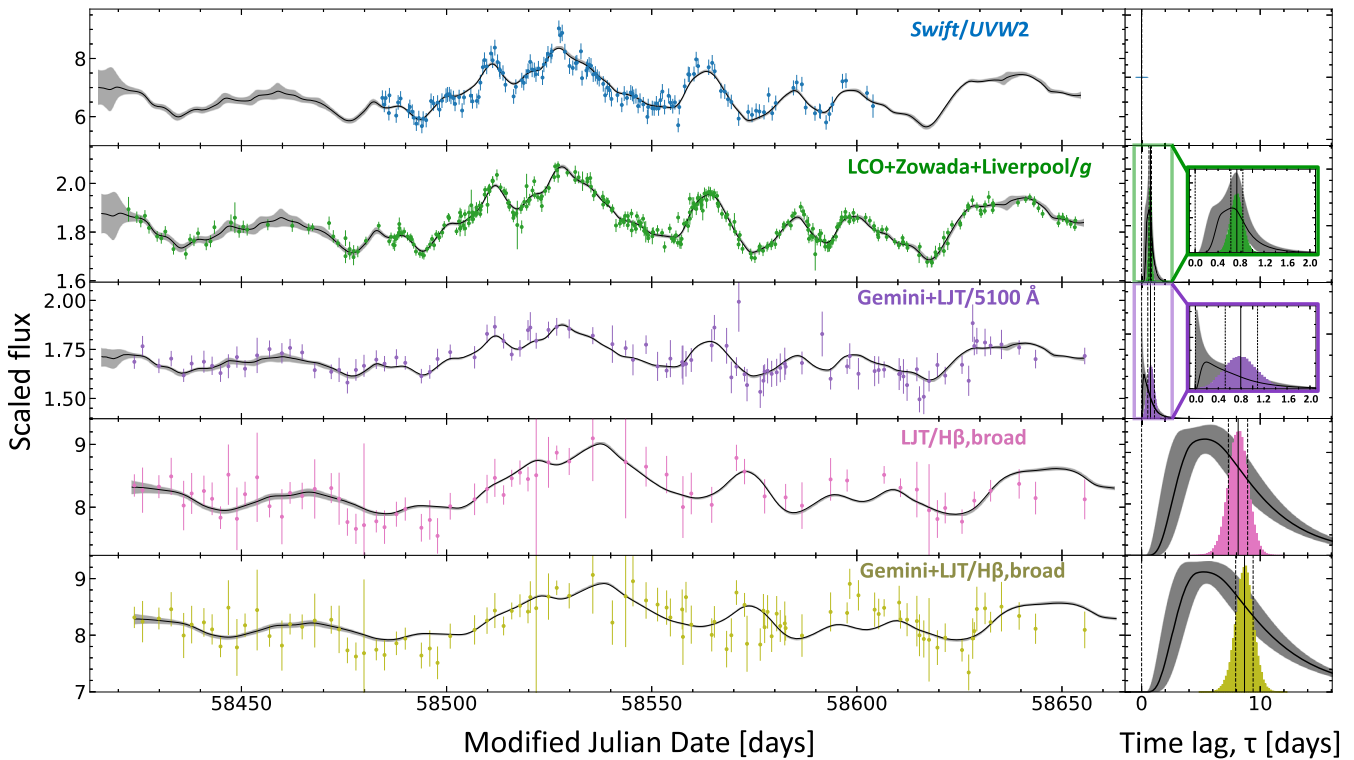


Figure 8. Time-lag measurements with reference to the Swift/*UVW2* band (top row) with lag distributions modeled as log-Gaussians. Left: the top three panels show continuum light curves—Swift/*UVW2* (blue), LCO+Zowada+Liverpool/*g* (green), and inter-calibrated Gemini+LJT/5100 Å—in units of 10^{-15} erg s $^{-1}$ cm $^{-2}$ Å $^{-1}$. The bottom two panels show the broad H β light curves—LJT only (pink) and Gemini+LJT inter-calibrated (olive)—in units of 10^{-14} erg s $^{-1}$ cm $^{-2}$ Å $^{-1}$. Right: time-lag distributions (colored histograms) for the mean lag and gray shaded uncertainty estimates from a log-Gaussian lag distribution of the light curves on the left with reference to the Swift/*UVW2* band, which has a fixed lag of 0.00 day. Insets in the second and the third panels show a close view of the time-lag distributions for LCO+Zowada+Liverpool/*g* and Gemini+LJT/5100 Å light curves, respectively. For each of the echo light curves, the black solid vertical line marks the lag measurement, given by the median lag of the colored distribution and the black dashed vertical lines (on either sides of the solid line) mark the corresponding uncertainty.

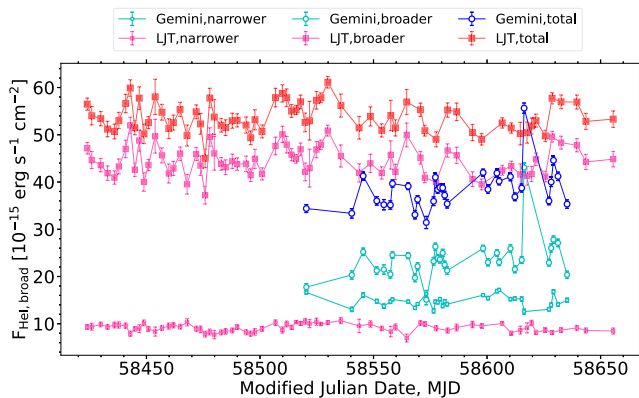


Figure 9. He I light curves highlighting the contributions from the individual broad components (referred to as broader and narrower) to the total broad components from Gemini (open circles) and LJT (solid squares) data. The smaller (larger) size of the markers represents narrower (broader) components. It is interesting to note that the broader He I light curve from the LJT spectra is brighter than the broader He I component from the Gemini spectra likely due to the blue wing of He I (traced primarily by the broader component) in the LJT data affected by instrumental broadening.

Eddington AGN, where self-shadowing effects due to a slim-disk structure in super-Eddington AGNs could result in the broad-line profiles appearing more Lorentzian than Gaussian. We recognize that our Mrk 142 spectral fitting model does not align with that of Wang et al. (2014b); however, our results are

not sufficient evidence to rule out the self-shadowing hypothesis. A detailed analysis of spectral line profiles for a larger sample of super-Eddington AGNs is required to build a robust understanding of how the accretion-disk behavior affects the observed broad-line profiles in these objects. We employed fixed narrow-line flux ratios $F_{H\beta}/F_{[O III] \lambda 5008}$ and $F_{He I}/F_{[O III] \lambda 5008}$ for the LJT spectral model (determined from flexible flux ratios for the Gemini spectra) due to the instrumental broadening in the LJT spectra affecting emission-line measurements. Although the LJT rms spectrum shows a weak feature at the He I location, PrepSpec modeling and light-curve analysis suggested that there is no adequate variability in the line that is measurable with the current Gemini+LJT data. However, we acknowledge that the He I emission line shows a peculiar profile evident from the high S/N of the Gemini spectra. The broader Gaussian used for the line indicates stronger blueshifted emission than the redshifted side of the line. Also, the He II line specifically required a broad, blueshifted component to accurately trace the emission in that region. Followed by spectral analysis, we empirically measured the FWHM values as well as calculated the narrow- and broad-line flux values of the H β and He I lines to obtain their light curves.

Applying PyROA, we performed cross-correlation analysis with continuum (Swift/*UVW2*, LCO+Zowada+Liverpool/*g*, and Gemini+LJT/5100 Å) and broad H β light curves (LJT and Gemini+LJT inter-calibrated) with a goal of determining reverberation time lag for the Gemini+LJT inter-calibrated

Table 7
[O III] λ 5008 Emission-line Measurements for LJT Spectra

Epoch	Position _{[O III]λ5008} (Å)	FWHM _{[O III]λ5008} (km s ⁻¹)	$F_{[O III]\lambda 5008}$ (10 ⁻¹⁵ erg s ⁻¹ cm ⁻²)	χ^2_{ν} ^a
1	5007.25 ± 0.09	718 ± 9	16.6 ± 0.2	2.27
2	5007.22 ± 0.13	754 ± 22	17.5 ± 0.4	1.45
3	5007.25 ± 0.13	741 ± 13	17.2 ± 0.3	2.00
4	5007.40 ± 0.12	787 ± 19	17.8 ± 0.4	2.03
5	5007.33 ± 0.10	716 ± 18	16.1 ± 0.4	2.07
6	5007.43 ± 0.13	740 ± 21	16.4 ± 0.4	1.71
7	5007.44 ± 0.16	880 ± 6	19.6 ± 0.4	1.60
8	5007.46 ± 0.06	691 ± 13	16.9 ± 0.3	2.56
9	5007.42 ± 0.10	679 ± 19	17.1 ± 0.3	1.68
10	5007.51 ± 0.17	707 ± 27	17.4 ± 0.6	1.28
11	5007.43 ± 0.14	742 ± ...	17.6 ± 0.3	1.51
12	5007.26 ± 0.09	713 ± 10	16.7 ± 0.3	2.19
13	5007.41 ± 0.20	716 ± 27	17.2 ± 0.6	1.51
14	5007.49 ± 0.12	757 ± 13	16.8 ± 0.3	1.67
15	5007.57 ± 0.14	737 ± 22	16.8 ± 0.4	1.42
16	5007.53 ± 0.10	682 ± 16	17.4 ± 0.3	1.66
17	5007.44 ± 0.10	682 ± 2	15.7 ± 0.2	1.98
18	5007.46 ± 0.15	736 ± 27	16.3 ± 0.5	1.20
19	5007.65 ± 0.14	752 ± 15	16.6 ± 0.3	1.93
20	5007.45 ± 0.15	727 ± 28	17.2 ± 0.6	1.24
21	5007.53 ± 0.14	758 ± 17	17.1 ± 0.4	1.40
22	5007.67 ± 0.17	802 ± 16	17.1 ± 0.4	1.47
23	5007.16 ± 0.23	772 ± 26	17.7 ± 0.7	1.21
24	5007.56 ± 0.10	674 ± 17	16.5 ± 0.3	1.74
25	5007.57 ± 0.11	700 ± 26	16.9 ± 0.4	1.66
26	5007.55 ± 0.11	733 ± 14	17.1 ± 0.3	1.77
27	5007.45 ± 0.09	680 ± 4	16.8 ± 0.3	2.02
28	5007.66 ± 0.14	801 ± 6	16.9 ± 0.3	1.45
29	5007.48 ± 0.10	785 ± 16	18.6 ± 0.3	1.96
30	5007.60 ± 0.14	742 ± 22	17.7 ± 0.5	1.34
31	5007.46 ± 0.10	707 ± 11	16.1 ± 0.3	2.25
32	5007.38 ± 0.08	699 ± 5	16.3 ± 0.4	1.32
33	5007.48 ± 0.13	684 ± 17	16.5 ± 0.4	1.80
34	5007.52 ± 0.11	683 ± 17	17.1 ± 0.4	1.76
35	5007.38 ± 0.11	776 ± 15	16.8 ± 0.3	2.82
36	5007.39 ± 0.06	681 ± 2	16.5 ± 0.2	4.36
37	5007.44 ± 0.09	682 ± 0	16.5 ± 0.2	2.13
38	5007.66 ± 0.13	810 ± 9	17.3 ± 0.4	1.47
39	5007.65 ± 0.24	719 ± 49	17.2 ± 1.0	2.02
40	5007.63 ± 0.12	719 ± 16	16.9 ± 0.4	1.71
41	5007.56 ± 0.08	728 ± 9	16.9 ± 0.2	4.65
42	5007.61 ± 0.09	688 ± 2	16.9 ± 0.2	3.74
43	5007.41 ± 0.14	713 ± 27	17.2 ± 0.5	1.52
44	5007.48 ± 0.16	712 ± 45	17.4 ± 0.9	1.63
45	5007.51 ± 0.13	745 ± 18	18.3 ± 0.4	1.53
46	5007.47 ± 0.10	731 ± 14	16.8 ± 0.3	1.98
47	5007.57 ± 0.22	744 ± 36	16.5 ± 0.7	1.05
48	5007.60 ± 0.12	685 ± 26	16.1 ± 0.5	2.26
49	5008.33 ± 0.21	857 ± 30	18.8 ± 0.6	2.06
50	5007.51 ± 0.09	691 ± 31	17.1 ± 0.5	3.21
51	5007.76 ± 0.08	726 ± 11	16.7 ± 0.2	3.28
52	5007.64 ± 0.12	686 ± 31	16.1 ± 0.5	1.61
53	5007.44 ± 0.11	707 ± 19	17.1 ± 0.4	1.82
54	5007.64 ± 0.11	679 ± 15	16.6 ± 0.4	1.59
55 ^b	5007.50 ± 0.23	670 ± 26	14.5 ± 0.6	1.97
56	5007.40 ± 0.12	646 ± 31	15.8 ± 0.4	1.53
57	5007.39 ± 0.08	634 ± 1	16.1 ± 0.2	2.55
58	5007.55 ± 0.08	711 ± 8	17.4 ± 0.2	3.54
59	5007.62 ± 0.08	724 ± 12	17.7 ± 0.3	3.37
60	5007.57 ± 0.16	726 ± 21	17.5 ± 0.5	1.48
61	5007.39 ± 0.14	668 ± 27	17.2 ± 0.6	1.50
62	5007.60 ± 0.13	750 ± 14	18.6 ± 0.3	2.58
63	5007.68 ± 0.09	659 ± 14	16.4 ± 0.3	2.02

Table 7
(Continued)

Epoch	Position _{[O III]λ5008} (Å)	FWHM _{[O III]λ5008} (km s ⁻¹)	$F_{[O III]λ5008}$ (10 ⁻¹⁵ erg s ⁻¹ cm ⁻²)	χ^2_ν ^a
64	5007.32 ± 0.08	660 ± 11	16.4 ± 0.3	3.39
65	5007.70 ± 0.08	727 ± 12	17.4 ± 0.2	3.46
66	5007.55 ± 0.09	681 ± 12	17.1 ± 0.3	2.27
67	5007.63 ± 0.10	709 ± 14	17.0 ± 0.3	2.03
68	5007.70 ± 0.10	756 ± 3	17.4 ± 0.3	1.73
69	5007.59 ± 0.17	752 ± 25	17.3 ± 0.4	1.78

Notes.

^a Reduced χ^2 , $\chi^2_\nu = \chi^2/\nu$, where ν indicates 1071 degrees of freedom, gives the model statistic for individual epochs.

^b This spectrum appeared very noisy likely due to some disturbance in the field of view at the time of observation. Therefore, we excluded this epoch from further analysis.

(This table is available in machine-readable form.)

H β light curve. PyROA provided an improvement in quantifying the uncertainties compared to previous studies. Most early RM studies have extensively applied the ICCF method for time-lag measurements, which makes it a good comparison standard. However, ICCF struggles with nonuniformly sampled data, which is true for our Gemini+LJT campaigns similar to most other studies, and uses linear interpolation to estimate the light-curve behavior in the regions with data gaps. Consequently, the uncertainties reported for ICCF-based measurements are typically conservative compared to JAVELIN and PyROA, as noted in this work for the 5100 Å continuum as well as the H β emission from LJT and Gemini+LJT inter-calibrated data (see Table 10). In the context of the uncertainties on time-lag measurements, JAVELIN has been shown to perform better. For instance, Edelson et al. (2019) reported uncertainties from ICCF to be twice as large as those from JAVELIN, which is also evident from the results in this work (see Table 10). JAVELIN uses damped random walk (DRW) to estimate the light-curve pattern in the regions where data are not available. DRW closely characterizes the variability observed in AGNs, plausibly leading to smaller uncertainties in the final lag measurements. However, JAVELIN requires a good estimation of uncertainties in data. For suboptimally calibrated uncertainties, JAVELIN can sometimes fail to deliver reliable lag measurements (Donnan et al. 2021). This is likely the reason the LJT/H β and Gemini+LJT/H β emission-line light curves, which have larger calibrated uncertainties than the continuum light curves, show time-lag measurements differing from those reported by PyROA. PyROA offers an improvement over JAVELIN—the ROA along with a robust error treatment not only prevents the outlier points from disrupting the estimation of the driving light curve but also applies a valid algorithm for resolving data gaps.

We measured a time lag of $8.68^{+0.75}_{-0.72}$ days for the Gemini+LJT inter-calibrated H β emission with reference to the UVW2 continuum. We also obtained a lag of $0.79^{+0.27}_{-0.29}$ days for the 5100 Å continuum with reference to the UVW2 band (that is consistent, within uncertainties, with the time lag–wavelength relationship in Cackett et al. 2020), and a lag of 7.89 ± 0.80 days for the H β emission with respect to the 5100 Å continuum. From here, we report a black hole mass of

$\log(M/M_\odot) = 6.28 \pm 0.29$ derived using Equation (1),

$$M = \frac{f c \tau_{H\beta} V_{FWHM,H\beta}^2}{G} \quad (1)$$

where we used a $\log(f)$ value of $-0.36^{+0.33}_{-0.54}$ from the dynamical modeling of the Mrk 142 BLR by Li et al. (2018). It is possible that the value of $\log(f)$ has a large uncertainty, which depends on the BLR’s dynamical model or the calibration using the $M-\sigma_*$ relation for classical bulges and pseudobulges (e.g., Ho & Kim 2014; Li et al. 2018; Yu et al. 2020). For V_{FWHM} , we used the mean H β FWHM of 1680 ± 14 km s⁻¹ from the Gemini spectra. Here, we chose the Gemini spectra due to their higher resolution providing a more reliable measurement of the narrower H β broad-line profile than the LJT spectra. We also considered the mean FWHM from the spectra as against the H β rms profiles as the rms spectra from Gemini were noisier blueward of the blue wing of the H β line. We further measured mean luminosities of $\log(L_{UVW2}) = 43.832 \pm 0.001$, $\log(L_{5100}) = 43.643 \pm 0.002$, and $\log(L_{H\beta}) = 41.621 \pm 0.002$. For the L_{5100} and $L_{H\beta}$ measurements, we adopted the mean flux value from our Gemini+LJT inter-calibrated light curves as their respective Gemini light curves alone were insufficient to provide a reliable flux scale due to the shorter observing timescale.

Our results agree with previously published measurements of Mrk 142 (Du et al. 2015; Li et al. 2018). From the previous 6 month SEAMBH campaign, Du et al. (2015) reported a time lag of $7.9^{+1.2}_{-1.1}$ days for H β with reference to 5100 Å. We measured an optical lag of 7.89 ± 0.80 days for H β in agreement with the Du et al. (2015) value within uncertainties. Furthermore, the derived black hole mass for Mrk 142 in this work, $\log(M/M_\odot) = 6.28 \pm 0.29$, agrees with the value reported in the recent velocity-resolved RM analysis by Li et al. (2018), $6.23^{+0.26}_{-0.45}$, within uncertainty limits. Table 11 summarizes the measured quantities in this work and shows their comparison with the values from previous studies.

To visualize our results in the broader context of reverberation-mapped AGNs, we placed the measured size of the H β line-emitting region on various $R-L$ scaling relations. Comparisons are discussed below.

Table 8
 $H\beta$ $\lambda 4861$ Emission-line Measurements for LJT Spectra

Epoch	FWHM $_{H\beta,b}$ (km s $^{-1}$)	$F_{H\beta,b}$ (10^{-15} erg s $^{-1}$ cm $^{-2}$)	FWHM $_{H\beta,n}$ (km s $^{-1}$)	$F_{H\beta,n}$ (10^{-15} erg s $^{-1}$ cm $^{-2}$)	FWHM $_{H\beta,t}$ (km s $^{-1}$)	$F_{H\beta,t}$ (10^{-15} erg s $^{-1}$ cm $^{-2}$)
1	1912 ± 52	83.5 ± 1.5	718 ± 9	4.85 ± 0.07	1660 ± 42	88.3 ± 1.5
2	1933 ± 73	82.7 ± 3.5	754 ± 22	5.13 ± 0.13	1702 ± 46	87.8 ± 3.5
3	1951 ± 38	83.3 ± 1.6	741 ± 13	5.03 ± 0.09	1748 ± 48	88.3 ± 1.6
4	1901 ± 52	84.9 ± 2.8	787 ± 19	5.22 ± 0.11	1700 ± 69	90.1 ± 2.8
5	1881 ± 46	80.3 ± 3.8	716 ± 18	4.72 ± 0.10	1706 ± 46	85.0 ± 3.8
6	1958 ± 85	82.2 ± 3.1	740 ± 21	4.80 ± 0.12	1708 ± 47	87.0 ± 3.1
7	2055 ± 86	82.6 ± 2.3	880 ± 6	5.74 ± 0.11	1750 ± 69	88.3 ± 2.3
8	1956 ± 54	81.3 ± 2.4	691 ± 13	4.95 ± 0.09	1804 ± 71	86.3 ± 2.4
9	1884 ± 63	78.3 ± 1.5	679 ± 19	5.02 ± 0.10	1618 ± 33	83.4 ± 1.5
10	1988 ± 85	85.2 ± 4.7	707 ± 27	5.10 ± 0.17	1742 ± 82	90.3 ± 4.7
11	1985 ± 102	78.2 ± 4.9	742 ± ...	5.17 ± 0.09	1647 ± 54	83.3 ± 4.9
12	1924 ± 44	82.1 ± 1.8	713 ± 10	4.90 ± 0.08	1703 ± 46	87.0 ± 1.8
13	1981 ± 87	84.8 ± 7.0	716 ± 27	5.03 ± 0.18	1848 ± 48	89.8 ± 7.0
14	2041 ± 64	80.2 ± 1.5	757 ± 13	4.93 ± 0.10	1779 ± 58	85.1 ± 1.5
15	2004 ± 57	78.5 ± 4.3	737 ± 22	4.94 ± 0.12	1684 ± 77	83.4 ± 4.3
16	2017 ± 83	82.3 ± 1.5	682 ± 16	5.11 ± 0.10	1630 ± 61	87.4 ± 1.5
17	1928 ± 64	81.8 ± 1.9	682 ± 2	4.61 ± 0.07	1702 ± 41	86.4 ± 1.9
18	1904 ± 79	82.9 ± 4.6	736 ± 27	4.77 ± 0.14	1678 ± 55	87.7 ± 4.6
19	2024 ± 63	83.0 ± 2.2	752 ± 15	4.87 ± 0.09	1782 ± 52	87.9 ± 2.2
20	1961 ± 91	81.3 ± 4.0	727 ± 28	5.05 ± 0.17	1657 ± 70	86.4 ± 4.0
21	1999 ± 68	77.6 ± 2.0	758 ± 17	5.02 ± 0.12	1696 ± 92	82.7 ± 2.0
22	1878 ± 92	76.6 ± 2.2	802 ± 16	5.01 ± 0.12	1685 ± 55	81.6 ± 2.2
23	1904 ± 60	77.1 ± 13.0	772 ± 26	5.18 ± 0.21	1755 ± 59	82.3 ± 13.0
24	1933 ± 44	77.7 ± 1.5	674 ± 17	4.83 ± 0.09	1653 ± 57	82.6 ± 1.5
25	1885 ± 73	76.8 ± 2.5	700 ± 26	4.96 ± 0.11	1647 ± 61	81.8 ± 2.5
26	2037 ± 49	78.9 ± 1.8	733 ± 14	5.02 ± 0.09	1816 ± 70	83.9 ± 1.8
27	1968 ± 76	79.7 ± 1.6	680 ± 4	4.92 ± 0.08	1735 ± 41	84.6 ± 1.6
28	1976 ± 77	76.7 ± 2.0	801 ± 6	4.94 ± 0.08	1764 ± 58	81.7 ± 2.0
29	1984 ± 45	78.0 ± 3.0	785 ± 16	5.46 ± 0.10	1742 ± 47	83.4 ± 3.0
30	1862 ± 89	75.4 ± 2.7	742 ± 22	5.18 ± 0.14	1698 ± 62	80.6 ± 2.7
31	2007 ± 39	80.2 ± 1.9	707 ± 11	4.71 ± 0.08	1744 ± 42	84.9 ± 1.9
32	2058 ± 96	81.3 ± 2.3	699 ± 5	4.77 ± 0.11	1741 ± 63	86.0 ± 2.3
33	1912 ± 56	82.9 ± 2.1	684 ± 17	4.84 ± 0.11	1688 ± 73	87.7 ± 2.1
34	1936 ± 39	84.7 ± 2.9	683 ± 17	5.00 ± 0.10	1726 ± 50	89.7 ± 2.9
35	1964 ± 29	81.9 ± 1.2	776 ± 15	4.91 ± 0.09	1730 ± 67	86.9 ± 1.2
36	1919 ± 32	84.6 ± 1.0	681 ± 2	4.85 ± 0.05	1702 ± 29	89.5 ± 1.0
37	1895 ± 76	85.5 ± 1.7	682 ± 0	4.82 ± 0.07	1654 ± 34	90.3 ± 1.7
38	1922 ± 72	84.5 ± 1.7	810 ± 9	5.08 ± 0.11	1708 ± 50	89.6 ± 1.7
39	1869 ± 69	85.1 ± 21.5	719 ± 49	5.05 ± 0.29	1655 ± 33	90.1 ± 21.5
40	1911 ± 50	87.1 ± 3.9	719 ± 16	4.94 ± 0.11	1670 ± 68	92.1 ± 3.9
41	1866 ± 45	88.7 ± 0.7	728 ± 9	4.96 ± 0.06	1641 ± 31	93.6 ± 0.7
42	1933 ± 47	87.3 ± 1.9	688 ± 2	4.96 ± 0.06	1682 ± 45	92.2 ± 1.9
43	1836 ± 74	91.0 ± 6.8	713 ± 27	5.03 ± 0.16	1700 ± 34	96.0 ± 6.8
44	1919 ± 58	87.2 ± 8.9	712 ± 45	5.10 ± 0.27	1686 ± 45	92.3 ± 8.9
45	1888 ± 66	86.5 ± 3.0	745 ± 18	5.36 ± 0.12	1676 ± 57	91.8 ± 3.0
46	1943 ± 46	85.2 ± 2.8	731 ± 14	4.94 ± 0.09	1663 ± 43	90.1 ± 2.8
47	1809 ± 133	80.0 ± 4.8	744 ± 36	4.85 ± 0.21	1606 ± 79	84.9 ± 4.8
48	1937 ± 54	82.2 ± 3.2	685 ± 26	4.71 ± 0.13	1700 ± 62	86.9 ± 3.2
49	2129 ± 115	80.4 ± 2.7	857 ± 30	5.51 ± 0.17	1702 ± 127	85.9 ± 2.7
50	2032 ± 39	87.9 ± 1.9	691 ± 31	5.02 ± 0.14	1773 ± 45	92.9 ± 1.9
51	1996 ± 36	85.7 ± 1.8	726 ± 11	4.89 ± 0.07	1749 ± 40	90.6 ± 1.8
52	1921 ± 51	81.7 ± 2.6	686 ± 31	4.73 ± 0.15	1665 ± 56	86.5 ± 2.6
53	1857 ± 43	81.6 ± 1.9	707 ± 19	5.00 ± 0.11	1667 ± 48	86.6 ± 1.9
54	1846 ± 71	80.3 ± 3.6	679 ± 15	4.87 ± 0.11	1627 ± 53	85.1 ± 3.6
55 ^a	2051 ± 101	98.8 ± 3.2	670 ± 26	4.24 ± 0.17	1837 ± 91	103.0 ± 3.2
56	1900 ± 60	84.4 ± 3.3	646 ± 31	4.64 ± 0.12	1657 ± 35	89.1 ± 3.3
57	1855 ± 32	84.3 ± 1.5	634 ± 1	4.71 ± 0.06	1673 ± 36	89.0 ± 1.5
58	1873 ± 45	85.1 ± 1.1	711 ± 8	5.11 ± 0.06	1648 ± 35	90.3 ± 1.1
59	1880 ± 33	83.1 ± 1.2	724 ± 12	5.18 ± 0.07	1683 ± 33	88.3 ± 1.2
60	1831 ± 79	82.8 ± 4.3	726 ± 21	5.13 ± 0.14	1674 ± 49	87.9 ± 4.3
61	1802 ± 71	79.5 ± 7.3	668 ± 27	5.04 ± 0.17	1536 ± 60	84.5 ± 7.3
62	1943 ± 57	78.1 ± 2.9	750 ± 14	5.44 ± 0.09	1724 ± 43	83.6 ± 2.9
63	1934 ± 51	79.9 ± 2.3	659 ± 14	4.81 ± 0.09	1639 ± 39	84.7 ± 2.3

Table 8
(Continued)

Epoch	FWHM _{Hβ,b} (km s ⁻¹)	$F_{H\beta,b}$ (10 ⁻¹⁵ erg s ⁻¹ cm ⁻²)	FWHM _{Hβ,n} (km s ⁻¹)	$F_{H\beta,n}$ (10 ⁻¹⁵ erg s ⁻¹ cm ⁻²)	FWHM _{Hβ,t} (km s ⁻¹)	$F_{H\beta,t}$ (10 ⁻¹⁵ erg s ⁻¹ cm ⁻²)
64	1852 ± 36	77.7 ± 1.7	660 ± 11	4.82 ± 0.07	1653 ± 37	82.5 ± 1.7
65	1893 ± 33	81.0 ± 1.1	727 ± 12	5.11 ± 0.07	1682 ± 46	86.2 ± 1.1
66	1930 ± 47	82.6 ± 1.5	681 ± 12	5.01 ± 0.09	1706 ± 32	87.6 ± 1.5
67	1877 ± 35	83.7 ± 2.2	709 ± 14	4.98 ± 0.09	1695 ± 56	88.7 ± 2.2
68	1838 ± 47	81.5 ± 2.4	756 ± 3	5.11 ± 0.09	1651 ± 43	86.6 ± 2.4
69	1893 ± 67	81.3 ± 3.0	752 ± 25	5.05 ± 0.11	1696 ± 35	86.3 ± 3.0

Notes. The second and the third columns providing the FWHM and flux values, respectively, for the broad (“b”) H β component include contributions from both the broad Gaussians defined for the line. The FWHM of the narrow (“n”) H β is equal to the FWHM of the [O III] λ 5008 (see Table 7, third column). The total (“t”) FWHM and flux include contributions from both the broad and the narrow components ($t = b + n$).

^a Excluded from further analysis. See note *a* in Table 7.

(This table is available in machine-readable form.)

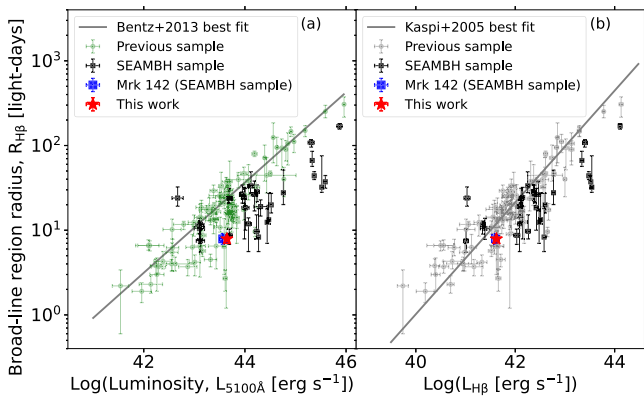


Figure 10. Radius–luminosity (R – L) scaling relations for H β in the optical including results from this work (red star). Panel (a): $R_{H\beta}$ – L_{5100} relation showing Mrk 142 from this work close to the Du et al. (2015) measurement (blue square). Panel (b): $R_{H\beta}$ – $L_{H\beta}$ relation showing Mrk 142 from this work overlapping with the measured value in Du et al. (2015). The SEAMBH objects (black squares; Du et al. 2014, 2015; Wang et al. 2014a; Hu et al. 2015; Li et al. 2018, 2021; Zhang et al. 2019) appear on the lower right of the gray solid lines, which represent the best-fit R – L relations from Bentz et al. (2013) with L_{5100} (panel (a)) and Kaspi et al. (2005) with $L_{H\beta}$ (panel (b)), indicating a smaller size for the BLR in highly accreting AGNs compared to the more typical, sub-Eddington AGNs mapped in previous studies (green circles, panel (a) and gray circles, panel (b); Stirpe et al. 1994; Santos-Lleó et al. 1997; Collier et al. 1998; Dietrich et al. 1998, 2012; Peterson et al. 1998, 2002, 2014; Kaspi et al. 2000, 2005; Santos-Lleó et al. 2001; Bentz et al. 2006, 2007, 2009a, 2009b, 2013, 2014; Collin et al. 2006; Denney et al. 2006, 2010; Grier et al. 2012; Barth et al. 2013; Pei et al. 2014, and references therein) at the same luminosities. In particular, the departure of Mrk 142 from the Bentz et al. (2013) best-fit relation in panel (a) is more apparent than the deviation from the Kaspi et al. (2005) relation in panel (b) (see the text for additional details).

Figure 10 shows the $R_{H\beta}$ – L_{5100} (panel (a)) and $R_{H\beta}$ – $L_{H\beta}$ (panel (b)) relations with the red star representing the Mrk 142 measurements from this work. In agreement with the findings from previous SEAMBH campaigns (black circles in Figure 10; see references in the figure caption), the red Mrk 142 star appears to depart from the general trend observed for typical RM objects, especially in the $R_{H\beta}$ – L_{5100} relation (green circles, panel (a); see the entire reference list in the figure caption). Comparatively, the departure of Mrk 142 from the Kaspi et al. (2005) best-fit relation (panel (b)) is less obvious. We quantified these Mrk 142 departures in terms of

time lag (along the vertical axis) relative to the standard deviation of the departures of the typical RM sample from both best-fit relations ($\sigma_{\text{departure}}$). While the departure of Mrk 142 from the Bentz et al. (2013) relation (15.7 lt-day) is $1.15\sigma_{\text{departure}}$ (where $\sigma_{\text{departure}} = 13.7$ lt-day), its departure from the Kaspi et al. (2005) relation (4.08 lt-day) is $\ll 1\sigma_{\text{departure}}$ (where $\sigma_{\text{departure}} = 26.8$ lt-day). The latter implies that $R_{H\beta}$ – $L_{H\beta}$ is a tighter relationship for AGNs than $R_{H\beta}$ – L_{5100} . The position of Mrk 142 in the $R_{H\beta}$ – L_{5100} relationship (panel (a)), considerably below the best-fit line, reiterates the characteristic of super-Eddington AGNs exhibiting smaller BLR sizes in contrast to the sub-Eddington population at the same luminosities (Du et al. 2016b). Du et al. (2015) tested this deviation of high accretion-rate AGNs from the $R_{H\beta}$ – L_{5100} relationship. Studying the differences in the BLR sizes for AGNs with low ($\dot{M}/\dot{M}_{\text{Edd}} < 3$) and high ($\dot{M}/\dot{M}_{\text{Edd}} \geq 3$) mass-accretion rates, Du et al. (2015) inferred that \dot{M} influences the size scales observed in super-Eddington AGNs, while such a correlation is absent in the low mass-accretion-rate objects.

Figure 11 shows the $R_{H\beta}$ – L_{5100} and $R_{H\beta}$ – L_{1350} scaling relations for NGC 5548 over time with optical lag measurements for H β , and luminosities at 5100 and 1350 Å (L_{1350}) from Eser et al. (2015). Again, the red star in both panels represents the Mrk 142 point from this work. Eser et al. (2015) formulated a conversion from L_{5100} to L_{1350} for NGC 5548 (see their Equation (4)) from all RM campaigns of the object from 1988–2008 (Peterson et al. 2002; Bentz et al. 2007, 2009b; Denney et al. 2010). We applied that conversion to calculate L_{1350} for NGC 5548 and generated the $R_{H\beta}$ – L_{1350} plot (Figure 11, panel (b)). Here, we extrapolated the Cackett et al. (2020) UV/optical imaging data—mean flux densities—in different bands assuming power-law behavior to estimate a luminosity of $\log(L_{1350}) = 44.13 \pm 0.03$ for Mrk 142 in this work (see Figure 12). The shift in the position of Mrk 142 from panels (a)–(b), closer to the R – L scaling relation in the UV, indicates that the UV emission is a better proxy for the ionizing continuum than the 5100 Å optical emission.

To further understand the comparison between the $R_{H\beta}$ – L_{1350} relations of Mrk 142 (a super-Eddington Seyfert 1 galaxy) and NGC 5548 (a normal Seyfert 1 galaxy), we compared their SEDs from the National Aeronautics and Space Administration/Infrared Processing and Analysis Center (NASA/IPAC) Extragalactic Database (NED) and recent studies, including Cackett et al. (2020). Figure 12 shows the

Table 9
He I $\lambda 5877$ Emission-line Measurements for LJT Spectra

Epoch	$\text{FWHM}_{\text{He } 1,b}$ (km s^{-1})	$F_{\text{He } 1,b}$ ($10^{-15} \text{ erg s}^{-1} \text{ cm}^{-2}$)	$\text{FWHM}_{\text{He } 1,n}$ (km s^{-1})	$F_{\text{He } 1,n}$ ($10^{-15} \text{ erg s}^{-1} \text{ cm}^{-2}$)	$\text{FWHM}_{\text{He } 1,r}$ (km s^{-1})	$F_{\text{He } 1,r}$ ($10^{-15} \text{ erg s}^{-1} \text{ cm}^{-2}$)
1	3321 ± 340	56.5 ± 1.3	718 ± 9	0.56 ± 0.01	3233 ± 310	57.0 ± 1.3
2	4215 ± 487	54.0 ± 1.9	754 ± 22	0.59 ± 0.01	3719 ± 432	54.6 ± 1.9
3	2677 ± 393	53.4 ± 1.5	741 ± 13	0.58 ± 0.01	2640 ± 335	54.0 ± 1.5
4	3526 ± 460	51.2 ± 1.6	787 ± 19	0.61 ± 0.01	3472 ± 439	51.8 ± 1.6
5	3672 ± 430	50.7 ± 1.5	716 ± 18	0.55 ± 0.01	2955 ± 380	51.2 ± 1.5
6	4021 ± 559	53.0 ± 1.7	740 ± 21	0.56 ± 0.01	3358 ± 509	53.6 ± 1.7
7	2800 ± 413	56.6 ± 1.9	880 ± 6	0.67 ± 0.01	2652 ± 370	57.3 ± 1.9
8	2393 ± 429	59.9 ± 1.8	691 ± 13	0.57 ± 0.01	2390 ± 356	60.5 ± 1.8
9	3007 ± 395	51.5 ± 1.5	679 ± 19	0.58 ± 0.01	3002 ± 377	52.1 ± 1.5
10	3440 ± 567	57.7 ± 2.4	707 ± 27	0.59 ± 0.02	3384 ± 534	58.3 ± 2.4
11	3742 ± 464	50.2 ± 2.0	742 ± ...	0.60 ± 0.01	3336 ± 414	50.8 ± 2.0
12	3707 ± 394	52.6 ± 1.3	713 ± 10	0.57 ± 0.01	3234 ± 349	53.1 ± 1.3
13	2031 ± 523	58.0 ± 3.7	716 ± 27	0.58 ± 0.02	2020 ± 440	58.6 ± 3.7
14	4636 ± 499	54.8 ± 1.7	757 ± 13	0.57 ± 0.01	3448 ± 477	55.3 ± 1.7
15	3570 ± 482	51.3 ± 2.1	737 ± 22	0.57 ± 0.01	3392 ± 451	51.9 ± 2.1
16	3777 ± 455	52.6 ± 1.6	682 ± 16	0.59 ± 0.01	2817 ± 387	53.2 ± 1.6
17	3086 ± 433	55.4 ± 1.5	682 ± 2	0.53 ± 0.01	3061 ± 378	55.9 ± 1.5
18	2644 ± 473	49.8 ± 2.2	736 ± 27	0.55 ± 0.02	2584 ± 432	50.4 ± 2.2
19	3681 ± 401	54.9 ± 1.5	752 ± 15	0.56 ± 0.01	3607 ± 366	55.4 ± 1.5
20	3500 ± 533	52.3 ± 2.2	727 ± 28	0.59 ± 0.02	3260 ± 504	52.9 ± 2.2
21	2511 ± 515	45.0 ± 1.9	758 ± 17	0.58 ± 0.01	2479 ± 447	45.6 ± 1.9
22	4378 ± 683	57.8 ± 2.1	802 ± 16	0.58 ± 0.01	3636 ± 586	58.4 ± 2.1
23	3628 ± 556	53.8 ± 3.7	772 ± 26	0.60 ± 0.02	3230 ± 523	54.4 ± 3.7
24	3526 ± 399	52.0 ± 1.4	674 ± 17	0.56 ± 0.01	3148 ± 367	52.6 ± 1.4
25	3227 ± 518	51.5 ± 1.7	700 ± 26	0.58 ± 0.01	3101 ± 485	52.1 ± 1.7
26	3575 ± 504	53.0 ± 1.6	733 ± 14	0.58 ± 0.01	3365 ± 459	53.5 ± 1.6
27	4302 ± 565	53.1 ± 1.4	680 ± 4	0.57 ± 0.01	4133 ± 484	53.6 ± 1.4
28	3591 ± 602	52.1 ± 1.7	801 ± 6	0.57 ± 0.01	3578 ± 529	52.6 ± 1.7
29	3724 ± 551	49.4 ± 1.5	785 ± 16	0.63 ± 0.01	3287 ± 540	50.0 ± 1.5
30	2501 ± 565	53.2 ± 2.1	742 ± 22	0.60 ± 0.02	2342 ± 479	53.8 ± 2.1
31	4400 ± 518	50.7 ± 1.4	707 ± 11	0.55 ± 0.01	4224 ± 445	51.3 ± 1.4
32	3186 ± 487	57.9 ± 2.0	699 ± 5	0.55 ± 0.01	3123 ± 437	58.4 ± 2.0
33	3456 ± 555	58.8 ± 1.8	684 ± 17	0.56 ± 0.01	3362 ± 519	59.3 ± 1.8
34	2880 ± 373	57.8 ± 1.9	683 ± 17	0.58 ± 0.01	2793 ± 302	58.4 ± 1.9
35	3257 ± 410	55.0 ± 1.3	776 ± 15	0.57 ± 0.01	3217 ± 374	55.6 ± 1.3
36	3778 ± 482	55.3 ± 0.9	681 ± 2	0.56 ± 0.01	3648 ± 431	55.8 ± 0.9
37	3369 ± 351	57.0 ± 1.4	682 ± 0	0.56 ± 0.01	3007 ± 302	57.5 ± 1.4
38	3024 ± 428	52.6 ± 2.0	810 ± 9	0.59 ± 0.01	3009 ± 400	53.2 ± 2.0
39	2901 ± 389	53.0 ± 4.1	719 ± 49	0.59 ± 0.03	2809 ± 349	53.5 ± 4.1
40	3124 ± 489	57.3 ± 1.8	719 ± 16	0.57 ± 0.01	3069 ± 431	57.9 ± 1.8
41	4761 ± 506	57.8 ± 1.0	728 ± 9	0.58 ± 0.01	3452 ± 380	58.4 ± 1.0
42	3699 ± 399	61.1 ± 1.2	688 ± 2	0.58 ± 0.01	3664 ± 382	61.7 ± 1.2
43	2720 ± 318	56.2 ± 2.4	713 ± 27	0.58 ± 0.02	2658 ± 296	56.8 ± 2.4
44	3220 ± 447	51.5 ± 2.4	712 ± 45	0.59 ± 0.03	3184 ± 440	52.1 ± 2.4
45	3481 ± 491	53.9 ± 2.0	745 ± 18	0.62 ± 0.01	3422 ± 444	54.5 ± 2.0
46	3367 ± 428	50.9 ± 1.4	731 ± 14	0.57 ± 0.01	3317 ± 417	51.5 ± 1.4
47	3618 ± 841	54.1 ± 3.2	744 ± 36	0.56 ± 0.02	3612 ± 762	54.6 ± 3.2
48	2302 ± 454	51.5 ± 1.7	685 ± 26	0.55 ± 0.02	2300 ± 404	52.0 ± 1.7
49	3621 ± 1008	56.9 ± 2.6	857 ± 30	0.64 ± 0.02	3598 ± 876	57.6 ± 2.6
50	3405 ± 461	55.3 ± 1.4	691 ± 31	0.58 ± 0.02	2868 ± 423	55.9 ± 1.4
51	2974 ± 379	50.9 ± 1.1	726 ± 11	0.57 ± 0.01	2512 ± 286	51.4 ± 1.1
52	3095 ± 465	49.0 ± 1.6	686 ± 31	0.55 ± 0.02	3061 ± 412	49.6 ± 1.6
53	3560 ± 386	55.2 ± 1.5	707 ± 19	0.58 ± 0.01	2853 ± 361	55.8 ± 1.5
54	4011 ± 529	54.9 ± 1.8	679 ± 15	0.56 ± 0.01	3867 ± 475	55.4 ± 1.8
55 ^a	1713 ± 519	56.2 ± 2.9	670 ± 26	0.49 ± 0.02	1708 ± 510	56.6 ± 2.9
56	3026 ± 343	50.5 ± 1.7	646 ± 31	0.54 ± 0.01	2986 ± 363	51.0 ± 1.7
57	3362 ± 424	49.0 ± 1.2	634 ± 1	0.55 ± 0.01	2803 ± 397	49.6 ± 1.2
58	3533 ± 224	52.5 ± 1.1	711 ± 8	0.59 ± 0.01	3401 ± 203	53.1 ± 1.1
59	4223 ± 565	51.4 ± 1.1	724 ± 12	0.60 ± 0.01	2775 ± 415	52.0 ± 1.1
60	2515 ± 545	50.3 ± 2.4	726 ± 21	0.60 ± 0.02	2515 ± 480	50.8 ± 2.4
61	3274 ± 521	50.4 ± 2.2	668 ± 27	0.59 ± 0.02	3129 ± 497	51.0 ± 2.2
62	3352 ± 421	51.9 ± 1.7	750 ± 14	0.63 ± 0.01	3337 ± 419	52.5 ± 1.7
63	3756 ± 487	53.0 ± 1.4	659 ± 14	0.56 ± 0.01	3257 ± 447	53.6 ± 1.4

Table 9
(Continued)

Epoch	FWHM _{He I,b} (km s ⁻¹)	$F_{\text{He I},b}$ (10 ⁻¹⁵ erg s ⁻¹ cm ⁻²)	FWHM _{He I,n} (km s ⁻¹)	$F_{\text{He I},n}$ (10 ⁻¹⁵ erg s ⁻¹ cm ⁻²)	FWHM _{He I,t} (km s ⁻¹)	$F_{\text{He I},t}$ (10 ⁻¹⁵ erg s ⁻¹ cm ⁻²)
64	4127 ± 1067	49.8 ± 1.2	660 ± 11	0.56 ± 0.01	3030 ± 761	50.3 ± 1.2
65	4321 ± 452	57.7 ± 1.2	727 ± 12	0.59 ± 0.01	3535 ± 420	58.3 ± 1.2
66	5320 ± 693	57.0 ± 1.4	681 ± 12	0.58 ± 0.01	3285 ± 608	57.6 ± 1.4
67	3695 ± 507	56.9 ± 1.5	709 ± 14	0.58 ± 0.01	3549 ± 504	57.5 ± 1.5
68	3375 ± 481	52.8 ± 1.7	756 ± 3	0.59 ± 0.01	2925 ± 432	53.4 ± 1.7
69	3431 ± 465	53.3 ± 1.7	752 ± 25	0.59 ± 0.01	2660 ± 385	53.9 ± 1.7

Notes. The second and the third columns providing the FWHM and flux values, respectively, for the broad (“b”) He I component include contributions from both the broad Gaussians defined for the line. The FWHM of the narrow (“n”) He I is equal to the FWHM of the [O III] λ 5008 (see Table 7, third column). The total (“t”) FWHM and flux include contributions from both the broad and the narrow components ($t = b + n$).

^a Excluded from further analysis. See note *a* in Table 7.

(This table is available in machine-readable form.)

Table 10
Time-lag Measurements

Time Lag (days)	PyROA ^a	ICCF	JAVELIN
UVW2-to-g	0.73 ^{+0.10} _{-0.10}	0.7 ^{+0.2} _{-0.2}	0.54 ^{+0.08} _{-0.08}
UVW2-to-5100 Å	0.79 ^{+0.27} _{-0.29}	1.7 ^{+1.8} _{-1.2}	0.78 ^{+0.42} _{-0.38}
UVW2-to-H β , LJT	8.14 ^{+0.82} _{-0.80}	8.8 ^{+2.5} _{-3.5}	6.95 ^{+0.69} _{-0.46}
UVW2-to-H β , Gemini+LJT	8.68 ^{+0.75} _{-0.72}	8.7 ^{+4.2} _{-9.1}	11.38 ^{+0.51} _{-4.49}

Note.

^a We consider these as the most robust time-lag measurements of the three methods. See Section 6 for further details.

Table 11
Comparison of Measurements to Previous SEAMBH Studies

Measured Quantity	This Work	Value From Previous SEAMBH Studies
$\tau_{\text{UVW2-to-H}\beta}$ ^a	8.68 ^{+0.75} _{-0.72} days	...
$\tau_{5100 \text{ \AA-to-H}\beta}$	7.89 ± 0.80 days	7.9 ^{+1.2} _{-1.1} days (Du et al. 2015)
$\log(M_*/M_\odot)$	6.28 ± 0.29	6.23 ^{+0.26} _{-0.45} (Li et al. 2018)
$\log(L_{\text{UVW2}})$ *	43.832 ± 0.001	...
$\log(L_{5100})$	43.643 ± 0.002	43.56 ± 0.06 (Du et al. 2015)
$\log(L_{\text{H}\beta})$	41.621 ± 0.002	43.56 ± 0.06 (Du et al. 2015)

Note.

^a New measurements.

SEDs for the above two AGNs from NED along with the derived optical-to-X-ray spectral slope (α_{ox}) of -1.35 ± 0.01 for Mrk 142 from the Cackett et al. (2020) observations (purple triangles representing mean flux densities in different bands). To derive the α_{ox} value, we: (1) fit the local SED around the 2500 Å data point assuming power-law behavior, (2) calculated the dereddened X-ray flux density at 2 keV, and (3) used Equation (1) for α_{ox} from Just et al. (2007). For NGC 5548, Merritt (2022) obtained an α_{ox} of -1.30 ± 0.04 from simultaneous X-ray/UV/optical observations. A less negative α_{ox} for NGC 5548 compared to Mrk 142 suggests a harder ionizing SED for the normal Seyfert 1 galaxy, likely due to the soft X-ray excess observed in the object (e.g., Mehdipour et al. 2015), than the super-Eddington AGNs. However, the soft excess in NGC 5548 was not evident in 2013, when an obscurer heavily absorbed its soft X-ray flux (Mehdipour et al. 2015).

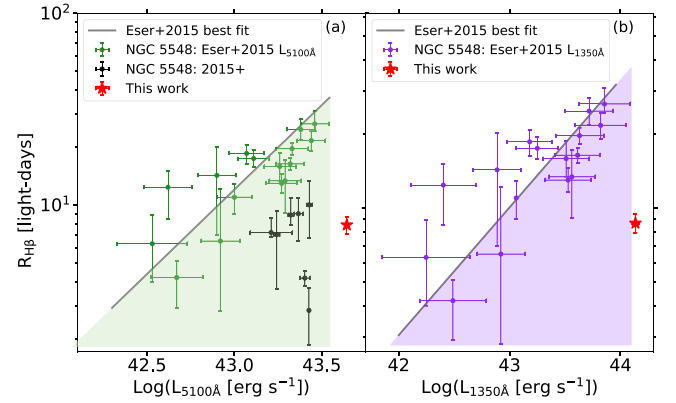


Figure 11. Multipepoch NGC 5548 radius–luminosity (R – L) scaling relations for H β in the optical and UV including luminosities from Eser et al. (2015) and results from this work (red star). Panel (a): NGC 5548 $R_{\text{H}\beta}$ – L_{5100} relation from (Eser et al. 2015; green circles) on which Mrk 142 from this work is located to the right at higher luminosities. This follows the similar deviation from the entire RM sample that is observed in Figure 10, panel (a). RM measurements for NGC 5548 post-2015 (Lu et al. 2016, 2022; Pei et al. 2017; De Rosa et al. 2018; black circles) are also included for completeness. Panel (b): $R_{\text{H}\beta}$ – L_{1350} relation for NGC 5548, including Mrk 142 from this work. From its position to the right of the Eser et al. (2015) best-fit R – L relation (gray solid line) with L_{5100} in panel (a), Mrk 142 has moved closer to the Eser et al. (2015) best-fit R – L relation with L_{1350} in panel (b), suggesting the UV as a better proxy for the driving continuum than the optical. In general, the offset of the SEAMBHs may reflect a different spectral energy distribution (SED).

Most Seyferts/quasars have some sort of soft X-ray excess; the debate for years has been over the origin (ionized disk reflection, warm Comptonized emission, a mixture, or both). The implication from Tortosa et al. (2023) is that for super-Eddington AGNs, ionized disk reflection can model the soft excess in this class of AGNs well. It is interesting to witness that despite their distinct types, the SED shapes of Mrk 142 and NGC 5547 are similar, as their α_{ox} values agree within uncertainties—a plausible explanation for the tighter $R_{\text{H}\beta}$ – L_{1350} correlation than $R_{\text{H}\beta}$ – L_{5100} noted in both the objects. Future accretion-disk modeling efforts can help understanding such comparisons of R – L relationships between normal and super-Eddington AGNs.

If UV emission is closer to the driving continuum as seen in Figure 11, this will affect the black hole mass of Mrk 142 derived from the 5100 Å to H β time lag. Recently, Cackett et al. (2020) performed the accretion-disk RM analysis for

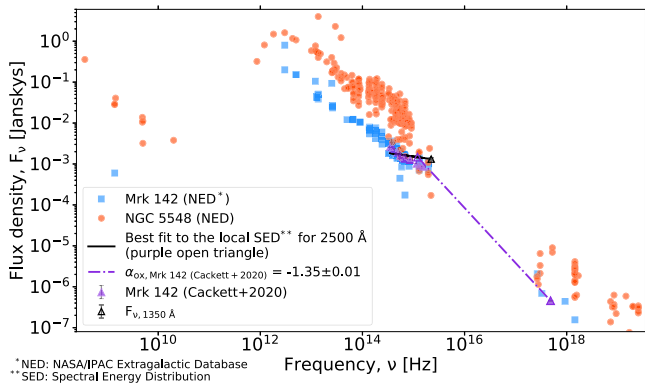


Figure 12. SEDs of Mrk 142 from the National Aeronautics and Space Administration/Infrared Processing and Analysis Center (NASA/IPAC) Extragalactic Database (NED, blue squares), and from Cackett et al. (2020, mean flux density in each band represented with purple triangles); and NGC 5548 from NED (orange circles) showing similar SED shapes for the two objects. We derived the optical-to-X-ray slope (α_{ox}) for the Mrk 142 data from Cackett et al. (2020) regarding a power-law behavior (fit indicated in black solid line) for the SED around the 2500 Å data point (purple open triangle). Results indicate a softer ionizing SED for Mrk 142 ($\alpha_{\text{ox}} = -1.35$) than NGC 5548 ($\alpha_{\text{ox}} = -1.30$; Merritt 2022); see the text for a detailed discussion. The fit to the Cackett et al. (2020) SED is extended to indicate the estimated 1350 Å data point (black open triangle) used in Figure 11.

Mrk 142 with data from Swift, LCO, Zowada, Liverpool, and other ground-based observatories, simultaneous to the Gemini +LJT data taken as a part of the same broader RM campaign. Cackett et al. (2020) pointed that if the *UVW2* band represents the driving continuum, then the black hole mass derived from the $H\beta$ optical lag is underestimated by $\sim 10\%$. We used the *UVW2* to $H\beta$ time lag result from this work to calculate the black hole mass in Mrk 142. We obtained a mass of $\log(M/M_{\odot}) = 6.32 \pm 0.29$ based on the *UVW2* to $H\beta$ time lag. This value is $\sim 10\%$ greater than the black hole mass derived by assuming 5100 Å as the driving continuum band, and thus verifies the discrepancy estimated by Cackett et al. (2020). This discrepancy would be as high as $\sim 40\%$ if X-rays, instead of UV, were the driving continuum (Cackett et al. 2020). However, our work does not propose any new implications to the accretion-disk structure of Mrk 142. A robust $H\beta$ lag measurement with reference to the X-ray continuum from future studies will help understand how X-rays play a role in driving the continuum variability in Mrk 142 and shape its inner accretion disk.

7. Conclusion

We performed BLR RM analysis of Mrk 142 with medium- and low-resolution optical spectra from Gemini and LJT, simultaneous to the Swift and LCO+Zowada+Liverpool photometric campaigns reported by Cackett et al. (2020) to measure the UV lag for $H\beta$ emission line. With *PrepSpec*-analysis, we corrected calibration discrepancies for both the Gemini and the LJT spectra individually. From spectral modeling in *Sherpa*, we measured FWHM and fluxes for [O III] $\lambda\lambda 4960, 5008$; $H\beta$ $\lambda 4861$; and He I $\lambda 5877$ emission lines. To combine the 5100 Å and $H\beta$ light curves from Gemini and LJT, we inter-calibrated the respective light curves from the two telescopes in *PyROA*. Applying *PyROA* for time-lag analysis, we measured a UV time lag for $H\beta$ and further derived refined black hole masses. Placing our results on various R - L scaling relations, we verified that our results are

consistent with previously published values for Mrk 142. We summarize our main findings below.

1. *PyROA*, using the Bayesian information criterion to evaluate model performance along with a rigorous treatment of uncertainties, provided a robust method for measuring cross-correlation time lags. This project is one of the early works employing the *PyROA* technique for measuring RM time lags with real data. In this process, the longer timescale of LJT spectra nicely complemented the gaps in the Gemini observations.
2. We measured, for the first time, a UV time lag of $8.68^{+0.75}_{-0.72}$ days for $H\beta$ in Mrk 142, with simultaneous photometry in the Swift/*UVW2* band and optical spectroscopy with Gemini and LJT. Assuming the UV continuum as the primary driver of the observed variability, we derived a black hole mass of $\log(M/M_{\odot}) = 6.32 \pm 0.29$.
3. We obtained a 5100 Å to $H\beta$ time lag of 7.89 ± 0.80 days, consistent with the measured value from previous SEAMBH campaigns (Du et al. 2015). From this lag measurement, we also derived a black hole mass for Mrk 142 of $\log(M/M_{\odot}) = 6.28 \pm 0.29$, in agreement with the mass reported by Li et al. (2018).
4. We placed the 5100 Å to $H\beta$ time lag with measured L_{1350} on the $R_{H\beta}$ - L_{1350} relation for NGC 5548 (Eser et al. 2015). Mrk 142 falls closer to the $R_{H\beta}$ - L_{1350} scaling relation than the $R_{H\beta}$ - L_{5100} relation indicating that the UV is closer to the “true” driving continuum as opposed to the 5100 Å band.

In addition, we also recorded supplementary results. Our spectral analysis indicated blueshifted, broad components for the He I and He II emission lines suggestive of wind components in these higher-ionization lines. To infer the cause of such disk+wind components, we need more higher-resolution data and BLR modeling efforts for super-Eddington AGNs. We intend to study the He I and He II lines in further detail in future work. Furthermore, BLR RM analysis with the concurrent X-ray data available from Swift can better inform our understanding of the measured $H\beta$ time lags with respect to the UV continuum. We aim to explore this in future study.

Acknowledgments

We recognize the support of Rick Edelson in taking the g -band data from Las Cumbres Observatory. V.C.K. acknowledges the support of Joel Roediger and the Gemini Observatory staff during the planning of observations and reduction of the Gemini data. V.C.K. thanks T. A. Boroson, who provided the Fe II template to C.H. for the spectral modeling process. We acknowledge the support of the Natural Sciences and Engineering Research Council of Canada (NSERC), Discovery Grant RGPIN/04157. V.C.K. acknowledges the support of the Ontario Graduate Scholarships. E.M.C. gratefully acknowledges support for analysis of the Swift data from NASA through grant 80NSSC19K0150, and support for analysis of the Zowada Observatory data from the NSF through grant AST-1909199. C.H. acknowledges support from the National Science Foundation of China (12122305). The research of V.C.K. was partially supported by the New Technologies for Canadian Observatories, an NSERC CREATE program. V.C.K. also acknowledges Jonathan Trump, Martin Houde,

Stanimir Metchev, and Charles McKenzie for their valuable feedback and discussions.

This research was based on observations obtained at the Gemini Observatory (processed using the Gemini IRAF package), which is managed by the Association of Universities for Research in Astronomy (AURA) under a cooperative agreement with the National Science Foundation on behalf of the Gemini Observatory partnership: the National Science Foundation (United States), National Research Council (Canada), Agencia Nacional de Investigación y Desarrollo (Chile), Ministerio de Ciencia, Tecnología e Innovación (Argentina), Ministério da Ciência, Tecnologia e Inovações e Comunicações (Brazil), and Korea Astronomy and Space Science Institute (Republic of Korea). This work was enabled by observations made from the Gemini North telescope, located within the Maunakea Science Reserve and adjacent to the summit of Maunakea. We are grateful for the privilege of observing the Universe from a place that is unique in both its astronomical quality and its cultural significance.

This research used observations from the Lijiang 2.4 m Telescope funded by the Chinese Academy of Sciences (CAS) and the People’s Government of Yunnan Province. We acknowledge the support of the National Key R&D Program of China No. 2021YFA1600404, and the National Science Foundation of China (11833008, 11973029, 11991051, 11991054).

The Liverpool Telescope is operated on the island of La Palma by Liverpool John Moores University in the Spanish Observatorio del Roque de los Muchachos of the Instituto de Astrofísica de Canarias with financial support from the UK Science and Technology Facilities Council.

Facilities: Gemini:Gillett, YAO:2.4m, Swift, FTN, Zowada, Liverpool:2m.

Software: IRAF, Gemini IRAF, Python, Astropy (Astropy Collaboration et al. 2013), PrepSpec, Sherpa (Freeman et al. 2001; Burke et al. 2018), PyROA (Donnan et al. 2021), ICCF (Gaskell & Sparke 1986; Gaskell & Peterson 1987), JAVELIN (Zu et al. 2011, 2013).

Appendix

Gemini Spectral Reduction—Special Cases

This Section describes the special cases from the spectral reduction of the Mrk 142 Gemini Spectra that were either treated differently or discarded due to calibration issues.

1. Epoch 11 narrow-slit standard star spectra: The extracted spectrum from exposure 1 appeared to drop in flux and flatten shorter than (blueward of) $\sim 4740 \text{ \AA}$, whereas the exposure 2 spectrum was flat on both ends. While it was possible to recover the flat region of the exposure 1 spectrum, the one from exposure 2 was not suitable for further analysis and hence was discarded. Because the shape of the spectrum blueward of $\sim 4740 \text{ \AA}$ was not evident from the exposure 2 spectrum, we recovered the region from ~ 4520 to $\sim 4740 \text{ \AA}$ with reference to the mean wide-slit standard star spectrum (used as the reference to correct for slit losses). Consequently, only the region longer than (redward of) $\sim 4740 \text{ \AA}$ was corrected for slit losses with the spline fitting procedure. The former and the latter were then concatenated to obtain *only one* slitloss-corrected spectrum for epoch 11 from exposure 1. Note that the standard star spectrum

from exposure 1 was later used to calibrate the narrow-slit science spectrum from exposure 2.

2. Epoch 11, exposure 1 wide-slit standard star spectrum: Two bumps with bad data were recovered redward of $\sim 5900 \text{ \AA}$ with reference to the spectrum from exposure 2. However, the recovery is not reliable, as the two spectra had slightly different count levels.
3. Discarded wide-slit standard star spectra: the wide-slit standard star spectra from exposures 1, 1, and 2 of epochs 21, 22, and 25, respectively, showed bump-like features, which could not be recovered as the standard star spectra from the other exposure of the same epochs had different count levels. Therefore, the epochs/exposures listed here were discarded.
4. Correction of affected pixels or recovery of bump-like regions on or close to the emission lines of interest: a few science spectra showed bumpy features on or close to the emission lines of interest, He I $\lambda 5877$ and H β $\lambda 4861$. We attempted to recover the “true” shape of such regions with reference to the other exposure taken with the same slit on the same night. In most cases, the two exposures had similar count levels. However, spectral measurements from the recovered spectra with different count levels are less reliable and must be considered carefully. What follows is a list of the specific cases.

Epoch 13, exposure 2 narrow-slit spectrum: A large, downward bump with bad data from $\sim 5545 \text{ \AA}$ until the red wing of the He I emission line was recovered with reference to the exposure 1 spectrum. Spectra from both exposures had similar count levels.

Epoch 16 narrow-slit spectra: Spectra from both exposures showed partially overlapping bump-like features in the region blueward of the H β emission line. Because neither of the exposures could be used to recover the shape of the spectrum in the affected region, we recovered the shapes of both the spectra with reference to the mean wide-slit science spectrum (used as the reference to correct for slit losses). In the exposure 2 spectrum, the recovery extended until the blue wing of H β . Spectra from both exposures had similar count levels.

Epoch 21, exposure 2 narrow-slit spectrum: the bumpy region from ~ 4325 to $\sim 4740 \text{ \AA}$ was recovered with reference to exposure 1 with similar count levels. The recovered region extended until the tail end of the blue wing of H β .

Epoch 27, exposure 1 narrow-slit spectrum: A small bumpy region from until the blue wing of H β was recovered with reference to exposure 2 with similar count levels.

Epoch 28, exposure 1 narrow-slit spectrum: A 17-pixel wide region residual from sky subtraction on the blue wing of H β was replaced by simulated data values after linear interpolation in that region. However, this correction was affecting H β line measurements and hence was excluded from the analysis.

Epoch 30 narrow-slit spectra: Spectra from both exposures showed overlapping bump-like features in the region from ~ 4370 to $\sim 4685 \text{ \AA}$ that were recovered with reference to the mean wide-slit science spectrum. In the exposure 1 spectrum, another bumpy feature from the red wing of the [O III] emission line at $\sim 5008 \text{ \AA}$ was

recovered with reference to the exposure 2 spectrum with similar count levels.

Epoch 3, exposure 1 wide-slit spectrum: A bumpy feature on the blue wing of the He I line was recovered with reference to the exposure 2 spectrum, where both spectra had similar count levels. This is one of the brighter wide-slit spectra. However, it was not used to generate the mean wide-slit spectrum for slitloss correction.

Epoch 11, exposure 1 wide-slit spectrum: A spike, possibly residual of sky subtraction, on the blue side of the [O III] peak at $\sim 5008 \text{ \AA}$ was replaced by simulated data after linear interpolation in the affected region.






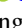






Epoch 14, exposure 2 wide-slit spectrum: A huge bump-like feature with bad data was replaced by simulated data after linear interpolation until the blue wing of $H\beta$.

Epoch 24, exposure 2 wide-slit spectrum: A huge bump with bad data extended from the region blueward of the He I line until the red end of the line. This affected region was recovered with reference to the exposure 1 spectrum, which was at slightly lower count levels than the exposure 2 spectrum.

Epoch 32, exposure 2 wide-slit spectrum: A bump-like feature from the blueward region of the He I line until the blue side of the He I peak was recovered with reference to the exposure 1 spectrum. Spectra from both exposures had similar count levels.

5. Epoch 25, exposure 2 narrow-slit science spectrum: The region on the blue side of He I $\lambda 5877$ emission line shows a large bumpy feature with bad data. Because the region redward of $\sim 5320 \text{ \AA}$ has lower count levels overall as compared to the spectrum from exposure 1, the affected region in spectrum 2 was not recovered. Therefore, this exposure was discarded.
6. Epoch 22, exposure 2 wide-slit science spectrum: The red end of the spectrum from ~ 6320 to $\sim 6400 \text{ \AA}$ was recovered with reference to the spectrum from exposure 1. However, the exposure 2 spectrum had slightly higher count levels than exposure 1.

ORCID iDs

Viraja C. Khatu  <https://orcid.org/0000-0002-0581-6506>
 Sarah C. Gallagher  <https://orcid.org/0000-0001-6217-8101>
 Keith Horne  <https://orcid.org/0000-0003-1728-0304>
 Edward M. Cackett  <https://orcid.org/0000-0002-8294-9281>
 Patrick Hall  <https://orcid.org/0000-0002-1763-5825>
 Jian-Min Wang  <https://orcid.org/0000-0001-9449-9268>
 Wei-Hao Bian  <https://orcid.org/0000-0002-2121-8960>
 Yan-Rong Li  <https://orcid.org/0000-0001-5841-9179>
 Pu Du  <https://orcid.org/0000-0002-5830-3544>
 Bo-Wei Jiang  <https://orcid.org/0000-0003-3825-0710>
 Sha-Sha Li  <https://orcid.org/0000-0003-3823-3419>
 Yu-Yang Songsheng  <https://orcid.org/0000-0003-4042-7191>
 Ming Xiao  <https://orcid.org/0000-0001-5981-6440>

References

- Abramowicz, M. A., Czerny, B., Lasota, J. P., & Szuszkiewicz, E. 1988, *ApJ*, 332, 646
- Astropy Collaboration, Robitaille, T. P., Tollerud, E. J., et al. 2013, *A&A*, 558, A33
- Baldwin, J. A., Phillips, M. M., & Terlevich, R. 1981, *PASP*, 93, 5
- Barth, A. J., Pancoast, A., Bennert, V. N., et al. 2013, *ApJ*, 769, 128
- Begelman, M. C. 2002, *ApJL*, 568, L97
- Bentz, M. C., Denney, K. D., Cackett, E. M., et al. 2006, *ApJ*, 651, 775
- Bentz, M. C., Denney, K. D., Cackett, E. M., et al. 2007, *ApJ*, 662, 205
- Bentz, M. C., Denney, K. D., Grier, C. J., et al. 2013, *ApJ*, 767, 149
- Bentz, M. C., Horenstein, D., Bazhaw, C., et al. 2014, *ApJ*, 796, 8
- Bentz, M. C., Peterson, B. M., Netzer, H., Pogge, R. W., & Vestergaard, M. 2009a, *ApJ*, 697, 160
- Bentz, M. C., Walsh, J. L., Barth, A. J., et al. 2009b, *ApJ*, 705, 199
- Blandford, R. D., & McKee, C. F. 1982, *ApJ*, 255, 419
- Boller, T., Brandt, W. N., & Fink, H. 1996, *A&A*, 305, 53
- Boroson, T. A., & Green, R. F. 1992, *ApJS*, 80, 109
- Brandt, W. N., & Alexander, D. M. 2010, *PNAS*, 107, 7184
- Bruzual, G., & Charlot, S. 2003, *MNRAS*, 344, 1000
- Burke, D., Laurino, O., Nguyen, D., et al. 2018, *sherpa/sherpa*: Sherpa, 4.10.0, v4.10.0, Zenodo, doi:10.5281/zenodo.1245678
- Cackett, E. M., Gelbord, J., Li, Y.-R., et al. 2020, *ApJ*, 896, 1
- Cackett, E. M., Horne, K., & Winkler, H. 2007, *MNRAS*, 380, 669
- Collier, S. J., Horne, K., Kaspi, S., et al. 1998, *ApJ*, 500, 162
- Collin, S., Kawaguchi, T., Peterson, B. M., & Vestergaard, M. 2006, *A&A*, 456, 75
- De Rosa, G., Fausnaugh, M. M., Grier, C. J., et al. 2018, *ApJ*, 866, 133
- Denney, K. D., Bentz, M. C., Peterson, B. M., et al. 2006, *ApJ*, 653, 152
- Denney, K. D., Peterson, B. M., Pogge, R. W., et al. 2010, *ApJ*, 721, 715
- Dietrich, M., Peterson, B. M., Albrecht, P., et al. 1998, *ApJS*, 115, 185
- Dietrich, M., Peterson, B. M., Grier, C. J., et al. 2012, *ApJ*, 757, 53
- Donnan, F. R., Horne, K., & Hernández Santisteban, J. V. 2021, *MNRAS*, 508, 5449
- Du, P., Hu, C., Lu, K.-X., et al. 2014, *ApJ*, 782, 45
- Du, P., Hu, C., Lu, K.-X., et al. 2015, *ApJ*, 806, 22
- Du, P., Lu, K.-X., Hu, C., et al. 2016a, *ApJ*, 820, 27
- Du, P., Lu, K.-X., Zhang, Z.-X., et al. 2016b, *ApJ*, 825, 126
- Du, P., Zhang, Z.-X., Wang, K., et al. 2018, *ApJ*, 856, 6
- Edelson, R., Gelbord, J., Cackett, E., et al. 2019, *ApJ*, 870, 123
- Eser, E. K., Vestergaard, M., Peterson, B. M., Denney, K. D., & Bentz, M. C. 2015, *ApJ*, 801, 8
- Fonseca Alvarez, G., Trump, J. R., Homayouni, Y., et al. 2020, *ApJ*, 899, 73
- Freeman, P., Doe, S., & Siemiginowska, A. 2001, *Proc. SPIE*, 4477, 76
- Gaskell, C. M., & Peterson, B. M. 1987, *ApJS*, 65, 1
- Gaskell, C. M., & Sparke, L. S. 1986, *ApJ*, 305, 175
- Grier, C. J., Peterson, B. M., Pogge, R. W., et al. 2012, *ApJ*, 755, 60
- Ho, L. C., & Kim, M. 2014, *ApJ*, 789, 17
- Hook, I. M., Jørgensen, I., Allington-Smith, J. R., et al. 2004, *PASP*, 116, 425
- Hu, C., Du, P., Lu, K.-X., et al. 2015, *ApJ*, 804, 138
- Jaroszyński, M., Abramowicz, M. A., & Paczynski, B. 1980, *AcA*, 30, 1
- Just, D. W., Brandt, W. N., Shemmer, O., et al. 2007, *ApJ*, 665, 1004
- Kaspi, S., Maoz, D., Netzer, H., et al. 2005, *ApJ*, 629, 61
- Kaspi, S., Smith, P. S., Netzer, H., et al. 2000, *ApJ*, 533, 631
- Leighly, K. M. 2004, *ApJ*, 611, 125
- Li, S.-S., Yang, S., Yang, Z.-X., et al. 2021, *ApJ*, 920, 9
- Li, Y.-R., Songsheng, Y.-Y., Qiu, J., et al. 2018, *ApJ*, 869, 137
- Lu, K.-X., Bai, J.-M., Wang, J.-M., et al. 2022, *ApJS*, 263, 10
- Lu, K.-X., Du, P., Hu, C., et al. 2016, *ApJ*, 827, 118
- Mehdipour, M., Kaastra, J. S., Kriss, G. A., et al. 2015, *A&A*, 575, A22
- Merritt, R. 2022, PhD thesis Georgia State Univ.
- Osterbrock, D. E., & Pogge, R. W. 1987, *ApJ*, 323, 108
- Pei, L., Barth, A. J., Aldering, G. S., et al. 2014, *ApJ*, 795, 38
- Pei, L., Fausnaugh, M. M., Barth, A. J., et al. 2017, *ApJ*, 837, 131
- Peterson, B. M. 1993, *PASP*, 105, 247
- Peterson, B. M. 2014, *SSRv*, 183, 253
- Peterson, B. M., Berlind, P., Bertram, R., et al. 2002, *ApJ*, 581, 197
- Peterson, B. M., Foltz, C. B., Byard, P. L., & Wagner, R. M. 1982, *ApJS*, 49, 469
- Peterson, B. M., Grier, C. J., Horne, K., et al. 2014, *ApJ*, 795, 149
- Peterson, B. M., Wanders, I., Horne, K., et al. 1998, *PASP*, 110, 660
- Planck Collaboration, Ade, P. A. R., Aghanim, N., et al. 2014, *A&A*, 571, A16
- Santos-Lleó, M., Chatzichristou, E., de Oliveira, C. M., et al. 1997, *ApJS*, 112, 271
- Santos-Lleó, M., Clavel, J., Schulz, B., et al. 2001, *A&A*, 369, 57
- Schlafly, E. F., & Finkbeiner, D. P. 2011, *ApJ*, 737, 103
- Shakura, N. I., & Sunyaev, R. A. 1973, *A&A*, 24, 337
- Shen, X., Hopkins, P. F., Faucher-Giguère, C.-A., et al. 2020, *MNRAS*, 495, 3252
- Steele, I. A., Smith, R. J., Rees, P. C., et al. 2004, *Proc. SPIE*, 5489, 679
- Stirpe, G. M., Winge, C., Altieri, B., et al. 1994, *ApJ*, 425, 609
- Tortosa, A., Ricci, C., Ho, L. C., et al. 2023, *MNRAS*, 519, 6267
- Vanden Berk, D. E., Richards, G. T., Bauer, A., et al. 2001, *AJ*, 122, 549

Véron-Cetty, M. P., Véron, P., & Gonçalves, A. C. 2001, [A&A](#), 372, 730
Wang, C.-J., Bai, J.-M., Fan, Y.-F., et al. 2019, [RAA](#), 19, 149
Wang, J.-M., Du, P., Hu, C., et al. 2014a, [ApJ](#), 793, 108
Wang, J.-M., Qiu, J., Du, P., & Ho, L. C. 2014b, [ApJ](#), 797, 65

Yu, L.-M., Bian, W.-H., Zhang, X.-G., et al. 2020, [ApJ](#), 901, 133
Zhang, Z.-X., Du, P., Smith, P. S., et al. 2019, [ApJ](#), 876, 49
Zu, Y., Kochanek, C. S., Kozłowski, S., & Udalski, A. 2013, [ApJ](#), 765, 106
Zu, Y., Kochanek, C. S., & Peterson, B. M. 2011, [ApJ](#), 735, 80